

# ERROR ESTIMATE BASED ADAPTIVE QUADRATURE FOR LAYER POTENTIALS OVER AXISYMMETRIC SURFACES

DAVID KRANTZ\* AND ANNA-KARIN TORNBERG†

**Abstract.** Layer potentials represent solutions to partial differential equations in an integral equation formulation. When numerically evaluating layer potentials at evaluation points close to the domain boundary, specialized quadrature techniques are required for accuracy because of rapid variations in the integrand. To efficiently achieve a specified error tolerance, we introduce an adaptive quadrature method with automatic parameter adjustment for axisymmetric surfaces, facilitated by error estimation. Notably, while each surface must be axisymmetric, the integrand itself need not be, allowing for applications with complex geometries featuring multiple axisymmetric bodies.

The proposed quadrature method utilizes so-called interpolatory semi-analytical quadrature in conjunction with a singularity swap technique in the azimuthal angle. In the polar angle, such a technique is used as needed, depending on the integral kernel, combined with an adaptive subdivision of the integration interval. The method is tied to a regular quadrature method that employs a trapezoidal rule in the azimuthal angle and a Gauss–Legendre quadrature rule in the polar angle, which will be used whenever deemed sufficiently accurate, as determined by a quadrature error estimate [C. Sorgentone and A.-K. Tornberg, *Advances in Computational Mathematics*, 49 (2023), p. 87].

Error estimates for both numerical integration and interpolation are derived using complex analysis, and are used to determine the adaptive panel subdivision given the evaluation point and desired accuracy. Numerical examples are presented to demonstrate the method’s efficacy.

**Key words.** Nearly singular, close evaluation, error control, integral equation, body of revolution, singularity swap quadrature

**1. Introduction.** Integral equation solvers for axisymmetric objects are of great importance in a variety of fields. For instance, the study of fluid-particle-systems at the microscale level, where the fluid flow is modeled by the Stokes equations, is vital for many industrial applications and fundamental fluid research. Applications include the rheology of fiber and polymer suspensions [22], suspensions of spheres [40], novel material development [26, 16], and self-assembly of biological or synthetic particles [20]. Axisymmetric particles, such as spheroids, rods, and rings, or segments of particles that can be described as bodies of revolution, are common in these applications. Numerical simulations of these systems are of significant interest, with integral equation methods demonstrating considerable success in this regard [36, 9, 4, 18, 47]. Additionally, axisymmetric objects are important in acoustic scattering and wave propagation, particularly in the design of sound-absorbing surfaces and modern high-power loudspeakers. Several integral equation-based solvers for the Helmholtz equation have been developed with this symmetry in mind [49, 35, 28]. However, accurate and efficient solution evaluations close to the surface of these objects, which is the focus of this work, remain an area of active research.

At the core of integral equation methods lie the fundamental solutions (Green’s functions) associated with the underlying partial differential equation. Here, the solution is represented as an integral, called a layer potential, over the boundary of the computational domain. This integral is a convolution of a Green’s function and a so-called layer “density” function. When a target (or an evaluation) point is close to the boundary, the integrand of the layer potential varies rapidly due to the Green’s function being evaluated near a singularity. Accurate evaluation of these nearly singular integrals is crucial not only for computing the solution given a known layer density but also when solving for the unknown layer density function if surfaces of different objects are close to each other. The challenge of resolving the integrand can to some extent be alleviated by upsampling, i.e. interpolating the layer density onto a finer grid where a regular quadrature rule is applied. However, as an evaluation point approaches a boundary, the required level of grid refinement increase dramatically. This demand underscores the necessity for specialized quadrature methods.

Our goal is accurate and efficient evaluation of layer potentials defined over smooth axisymmetric geometries. To this end, we have developed a special quadrature method, named the *singularity swap surface quadrature (S3Q)* method. Specifically, we consider a generic layer potential

$$(1.1) \quad u(\mathbf{x}) = \int_S \frac{k(\mathbf{x}, \mathbf{y})\sigma(\mathbf{y})}{\|\mathbf{y} - \mathbf{x}\|^{2p}} dS(\mathbf{y}), \quad p = 1/2, 3/2, \dots,$$

\*Department of Mathematics, KTH Royal Institute of Technology, Stockholm, Sweden (davkra@kth.se).

†Department of Mathematics, KTH Royal Institute of Technology, Stockholm, Sweden (akto@kth.se).

where the function  $k(\mathbf{x}, \mathbf{y})$  and layer density  $\sigma(\mathbf{y})$ , as well as the axisymmetric surface  $S \subset \mathbb{R}^3$ , are assumed to be given and smooth, and  $\mathbf{x} = (x, y, z) \in \mathbb{R}^3 \setminus S$ . In practice,  $\sigma(\mathbf{y})$  might only be known at discrete surface points, but we will make the assumption that it is well resolved on the surface grid. Since the target point  $\mathbf{x} \notin S$ , the integrand in (1.1) will not have a singularity, but the closer  $\mathbf{x}$  is to  $S$ , the more peaked it becomes due to the factor  $\|\mathbf{y} - \mathbf{x}\|^{-2p}$ .

To avoid unnecessary additional computational cost, we aim to activate the special quadrature method only when the fixed quadrature rule, based on the surface discretization, is insufficiently accurate. This fixed quadrature is often referred to as regular or smooth quadrature. In this work, for each  $\mathbf{x}$  and desired accuracy, we use the error estimates from [42] to determine when the special quadrature method should be employed. These estimates build upon a sequence of previous works, which we briefly overview here (a more detailed review is available in [3, Section 1]).

Consider the simple integral

$$(1.2) \quad \int_{-1}^1 \frac{1}{((t-a)^2 + b^2)^p} dt = \int_{-1}^1 \frac{1}{(t-z_0)^p (t-\bar{z}_0)^p} dt, \quad \begin{array}{l} z_0 = a + ib, \\ a, b \in \mathbb{R}, b > 0, p > 0. \end{array}$$

When  $b$  is small, this integral becomes nearly singular due to the integrand having singularities in the form of complex-conjugate poles for  $p \in \mathbb{Z}^+$  and otherwise branch points in the complex plane near the interval  $[-1, 1]$ . In [21], the quadrature error was expressed as a contour integral in the complex plane, involving the integrand and a so-called remainder function specific to the quadrature rule used. Building on this, Elliot et al. [23] derived quadrature error estimates for the Gauss–Legendre quadrature rule, incorporating a monomial in the numerator of (1.2). A significant advancement was made in [6], where this framework was extended to handle curved segments in the plane through a complex-variable formulation. The selection of branch cuts introduced in [23] was important in extending the analysis to smooth curves in  $\mathbb{R}^3$  [3]. To evaluate the error estimates, singularities in the complex parameter plane, similar to  $z_0$  and  $\bar{z}_0$  in (1.2), are identified as roots of a distance function. Additionally, [3] extended the analysis to two-dimensional surfaces in  $\mathbb{R}^3$ , discretized with either Gauss–Legendre quadrature on quadrilateral patches or the global trapezoidal rule. In [42], further modifications were made for spherical geometry parameterizations to obtain the error estimates used in this work.

Several special quadrature rules for accurate evaluation of nearly singular layer potentials exist in the literature and are briefly reviewed in the following. For two-dimensional problems, the time-tested interpolatory semi-analytical quadrature method of Helsing–Ojala [29] is widely regarded as the gold standard, with several adaptations [37, 38, 11] extending its utility (see also [27] for a review of other techniques). The more recent singularity swap quadrature (SSQ) method introduced in [2], and further developed in [1, 10], offers several advantages, most notably its extension to line integrals in three dimensions. The SSQ method is based on the concept of “swapping” the nearly singular factor for a simpler one with matching singularities in the complex parameter plane. Like interpolatory semi-analytical quadrature methods, SSQ expands a smooth factor of the integrand in some basis, and analytically integrates the product of each basis function with the remaining simpler nearly singular term. The analytical values of these integrals can often be found through recurrence formulas, although their stability can be a concern that necessitates additional techniques.

In three dimensions, special quadrature techniques remain an active research topic, especially for the nearly singular case. The quadrature by expansion (QBX) method [32, 12] was introduced in two dimensions, offering a natural extension to 3D. For 2D off-surface evaluations, [6] provided a parameter selection strategy for QBX, where upsampling rates were set from error estimates. As spherical harmonics expansions are used both for QBX and the fast multipole method in 3D, an integration of the two was envisioned. This proved however to be a complicated task, and it took considerable time before software was available for common equations like Laplace and Helmholtz [45]. Achieving the desired efficiency has been challenging due to the large number of expansion terms needed, despite significant improvements from using so-called target-specific expansions introduced in [41], which speed up near-field evaluations [46].

Another path to make efficient use of QBX has been taken for Stokes flow [4, 9], where target-specific quadrature weights for axisymmetric particles can be precomputed with reduced cost and storage, completely hiding the cost of QBX in the actual evaluation for target points on the surface. For off-surface target points, i.e. the nearly singular evaluation discussed in this paper, one can precompute to significantly reduce the

cost of obtaining the QBX coefficients (where each one will depend on the layer density in all discrete points for a global surface discretization), but the actual evaluation of the expansion must be made on the fly as the locations of the evaluation points are not known beforehand. This cost remains a bottleneck in simulations but could potentially be reduced by adopting a local panel-based discretization instead of a global one.

Another special quadrature method for three-dimensional problems is the so-called hedgehog method, also known as the line extrapolation/interpolation method [48, 8]. In this approach, the layer potential is evaluated at several sample points, each maintaining a minimum distance from the surface along a line in the domain, to ensure sufficiently accurate evaluations. These sample values are then extrapolated along the line towards the surface. If the value of the layer potential at the point where the line touches the surface is accessible, it can also be included when forming the approximation. However appealing in its simplicity, the achievable accuracy is strongly dependent on the extrapolation distance, and the method's non-trivial parameter selection makes it challenging to use optimally.

An alternate approach for accurately evaluating nearly singular integrals involves replacing the kernel with a regularized version defined by a length scale parameter,  $\delta$ . This enables the use of regular quadrature rules, followed by correction terms [43] or extrapolating the values of a few regularized integrals evaluations [13]. Typically,  $\delta$  should be chosen so that the regularization error dominates the discretization error. In [13], a fifth-order regularization for the Laplace and Stokes flow layer potentials was derived. By appropriately setting  $\delta$ , an error decay near the surface of approximately  $\mathcal{O}(h^5)$  was observed, where  $h$  is the three-dimensional grid spacing that covers the surface.

A promising method introduced in [50], and subsequently improved in [31], transforms surface integrals on boundary patches into a set of line integrals using Stokes' theorem. Although currently limited to Laplace layer potentials, this technique shows significant potential. For spherical geometries, an efficient quadrature scheme based on vectorial spherical harmonic basis functions was proposed in [19], offering an alternative for specialized cases.

In axisymmetric settings, considerable work has been devoted to developing integral equation solvers for Helmholtz equation, along with quadrature schemes tailored to these problems. In [49], a discrete Fourier transformation technique (FFT) is employed in the azimuthal direction, creating a number of Fourier integrals defined over the generating curve. These integrals are evaluated analytically using recursion relations. The authors note that these analytic formulas remain stable in regions where the FFT becomes inaccurate, an observation that likely stems from not addressing off-surface field evaluations. A major challenge in such scenarios is that the target point can lie anywhere within the computational domain. In the axial direction, a precomputed general-purpose Kolm-Rokhlin quadrature [33] was used. Helsing & Karlsson [28] significantly improved this method by incorporating highly accurate off-surface field evaluations. They introduced an analytic product integration scheme in the axial direction, based on [29], by analyzing the singular behavior of the integrand after integrating along the azimuthal direction. Additionally, they addressed the instabilities associated with the recurrence formulas for evaluating Fourier integrals heuristically. It should be noted that these integral equation-based solvers rely on the axisymmetric nature of the entire problem. While these quadrature schemes might theoretically extend to problems where only the geometries are axisymmetric, they remain untested in such contexts.

## 1.1. Preliminaries.

**1.1.1. Discretization.** Let  $S$  be a two-dimensional surface in  $\mathbb{R}^3$  parameterized by  $\gamma : E \rightarrow \mathbb{R}^3$ , where  $E = \{E_1 \times E_2\} \subset \mathbb{R}^2$ . This makes (1.1) take the form

$$(1.3) \quad u(\mathbf{x}) = \iint_E \frac{k(\mathbf{x}, \gamma(\theta, \varphi)) \sigma(\gamma(\theta, \varphi))}{\|\gamma(\theta, \varphi) - \mathbf{x}\|^{2p}} \left\| \frac{\partial \gamma}{\partial \theta} \times \frac{\partial \gamma}{\partial \varphi} \right\| d\varphi d\theta = \iint_E \frac{f(\theta, \varphi)}{\|\gamma(\theta, \varphi) - \mathbf{x}\|^{2p}} d\varphi d\theta,$$

where the function  $f(\theta, \varphi)$  contains all the smooth components, and implicitly depends on the target point  $\mathbf{x}$ . In this paper, we consider axisymmetric surfaces, where we primarily let  $E = E_1 \times E_2 = \{(\theta, \varphi) \in [0, \pi] \times [0, 2\pi)\}$ , yielding

$$(1.4) \quad \gamma(\theta, \varphi) = (a(\theta) \sin(\theta) \cos(\varphi), a(\theta) \sin(\theta) \sin(\varphi), b(\theta) \cos(\theta)),$$

where  $a(\theta) > 0$ ,  $b(\theta) > 0$ . Throughout this work, we will use the simple linear map  $\theta(t, \theta_a, \theta_b)$  to relate  $t \in [-1, 1]$  and the polar angle  $\theta \in [\theta_a, \theta_b]$  as needed,

$$(1.5) \quad \theta(t, \theta_a, \theta_b) = \frac{\theta_a + \theta_b}{2} + \theta_{\text{sc}} t, \quad \theta_{\text{sc}} = \frac{\theta_b - \theta_a}{2}.$$

The corresponding inverse mapping is defined as,

$$(1.6) \quad t(\theta, \theta_a, \theta_b) = \frac{1}{\theta_{\text{sc}}} \left( \theta - \frac{\theta_a + \theta_b}{2} \right).$$

When  $\theta_a = 0$  and  $\theta_b = \pi$ , we will use the shorter notation  $\theta(t)$  and  $t(\theta)$ .

Next, we introduce the squared-distance function for the surface  $\gamma(\theta, \varphi) = (\gamma_1(\theta, \varphi), \gamma_2(\theta, \varphi), \gamma_3(\theta, \varphi))$  and a target point  $\mathbf{x} = (x, y, z)$ ,

$$(1.7) \quad R^2(\theta, \varphi, \mathbf{x}) := \|\gamma(\theta, \varphi) - \mathbf{x}\|^2 = (\gamma_1(\theta, \varphi) - x)^2 + (\gamma_2(\theta, \varphi) - y)^2 + (\gamma_3(\theta, \varphi) - z)^2,$$

which makes (1.3) take the form

$$(1.8) \quad \mathcal{I}[\Theta_p](\mathbf{x}) = \mathcal{I}_t \mathcal{I}_\varphi [\Theta_p](\mathbf{x}) = \iint_E \Theta_p(\theta(t, \theta_a, \theta_b), \varphi, \mathbf{x}) \theta_{\text{sc}} \, d\varphi \, dt, \quad \Theta_p(\theta, \varphi, \mathbf{x}) = \frac{f(\theta, \varphi)}{(R^2(\theta, \varphi, \mathbf{x}))^p}.$$

Here, the notation  $\mathcal{I}_t$  and  $\mathcal{I}_\varphi$  indicate that the integral is taken in the  $t$  and  $\varphi$  direction, respectively. We will later use this, and similar, subscripts to distinguish if an operator is applied in the  $t$  or  $\varphi$  direction.

A natural way to discretize the integral with this parametrization is using an  $n_t$ -point Gauss–Legendre quadrature rule in the  $t$  direction on  $[-1, 1]$ , with quadrature nodes  $\{t_k\}_{k=1}^{n_t}$  and weights  $\{w_k^{\text{GL}}\}_{k=1}^{n_t}$ , and an  $n_\varphi$ -point trapezoidal rule in the  $\varphi$  direction, with nodes  $\{\varphi_\ell\}_{\ell=1}^{n_\varphi}$  and weights  $\{w_\ell^{\text{TZ}}\}_{\ell=1}^{n_\varphi}$ . Applying this tensor product quadrature to approximate (1.8) gives

$$(1.9) \quad \mathbf{Q}_{n_t, n_\varphi}[\Theta_p](\mathbf{x}) = \mathbf{Q}_{t, n_t} \mathbf{Q}_{\varphi, n_\varphi}[\Theta_p](\mathbf{x}) = \sum_{k=1}^{n_t} \sum_{\ell=1}^{n_\varphi} \frac{f(\theta(t_k), \varphi_\ell) w_\ell^{\text{TZ}} w_k^{\text{GL}} \theta_{\text{sc}}}{(R^2(\theta(t_k), \varphi_\ell, \mathbf{x}))^p}.$$

We refer to this as regular quadrature in both directions, with the quadrature error

$$(1.10) \quad |\mathbf{E}_{n_t, n_\varphi}[\Theta_p](\mathbf{x})| = \left| \mathcal{I}[\Theta_p](\mathbf{x}) - \mathbf{Q}_{n_t, n_\varphi}[\Theta_p](\mathbf{x}) \right|.$$

Figure 1.1 presents the measured quadrature error for the harmonic layer potentials over two prototype geometries and compares it to the corresponding error estimate computed according to [42], which we detail in Section 3.3. The color map illustrates the absolute value of the pointwise error, hereafter referred to as the absolute error, in  $\log_{10}$  scale. The results suggest that the error estimates perform sufficiently well; that is, given a desired accuracy of (1.8), they can be used to determine whether regular quadrature suffices for a given target point.

**1.1.2. Roots of  $R^2(\theta, \varphi, \mathbf{x})$ .** Since  $f$  is assumed to be smooth and  $\mathbf{x} \notin \gamma(\theta, \varphi)$ , the integrand of (1.8) will not be singular, but can be sharply peaked for  $\mathbf{x}$  close to  $\gamma(\theta, \varphi)$ . If we fix one parametrization variable, then the integrand has singularities in the complex plane of the other parameter that bounds its region of analyticity. Given a target point  $\mathbf{x}$  and fixed value of  $\theta \in E_1$ , the squared-distance function  $R^2(\theta, \varphi, \mathbf{x})$  introduced in (1.7), may have multiple complex-conjugate root pairs in  $\varphi^1$ . We focus on the pair closest to  $E_2$ , denoted  $\{\varphi_0(\theta, \mathbf{x}), \overline{\varphi_0(\theta, \mathbf{x})}\}$ , satisfying

$$(1.11) \quad R^2(\theta, \varphi_0(\theta, \mathbf{x}), \mathbf{x}) = R^2(\theta, \overline{\varphi_0(\theta, \mathbf{x})}, \mathbf{x}) = 0.$$

Similarly, by changing the role of  $\theta$  (or  $t$ ) and  $\varphi$ , the roots  $\{\theta(t_0(\varphi, \mathbf{x})), \overline{\theta(t_0(\varphi, \mathbf{x}))}\}$ , where  $t_0(\varphi, \mathbf{x})$  is the root of  $R^2(\theta(t), \varphi, \mathbf{x})$ , are those closest to  $E_1$ .

<sup>1</sup> $R^2(\theta, \varphi, \mathbf{x})$  is no longer a norm when evaluated with complex arguments, in which case we use the right-most expression in (1.7).



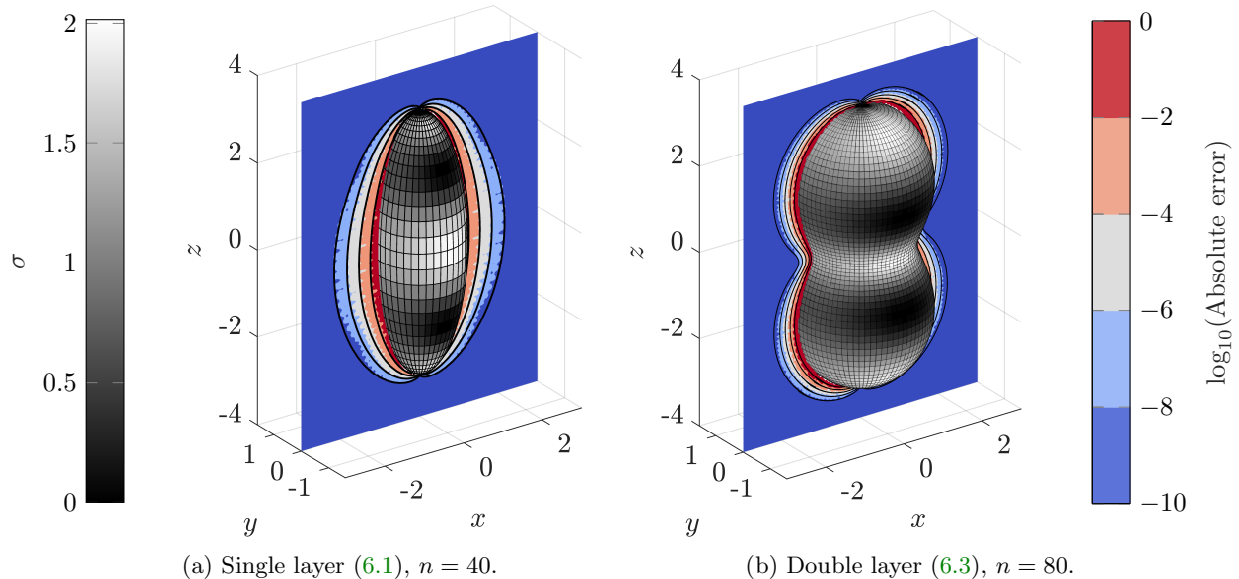


Fig. 1.1: Colors display the measured error (1.10) in  $\log_{10}$  scale, for the Laplace layer potentials, evaluated with  $n_t = n_\varphi = n$ , and only one interval in  $t$ . The solid black contour lines illustrating the error estimate from [42] at levels  $10^{-2}$ ,  $10^{-4}$ ,  $10^{-6}$ ,  $10^{-8}$  correspond well to the measured error. The layer density function is set to  $\sigma(\gamma(\theta, \varphi)) = \sin(5\theta)e^{-\cos^2(\varphi)} + 1.03$ .

These roots, along with those of other similar squared distance functions, are essential to the proposed quadrature method in Section 2, and in the error estimates derived in Section 3. For certain geometries, the roots can be determined analytically, but in general, they must be found through a one-dimensional numerical root-finding procedure. While the distance function does not have any roots in  $\varphi$  for evaluation points along the symmetry line of an axisymmetric particle, accurate error estimates can still be derived by analyzing appropriate limits of the analytical expressions for the roots [42].

**1.2. Contribution and outline.** The main contributions of this paper are the introduction of a new adaptive quadrature method, *singularity swap surface quadrature (S3Q)*, and the development of new quadrature and interpolation error estimates needed to automate parameter selection and algorithmic choices. The S3Q method evaluates nearly singular layer potentials in the form of (1.1) over smooth axisymmetric surfaces to high and controllable accuracy. Specifically, given the base surface discretization on which the layer density is assumed to be well resolved, the method features automatic parameter selection with the only required user-prescribed parameter being the desired accuracy. Users can optionally specify the order of the Gauss–Legendre quadrature rule for adaptive integration in the polar direction, which can have an effect on the efficiency of the scheme. In this paper, the S3Q method is used to evaluate the single and double layer potentials for harmonic potentials and Stokes flow.

The S3Q method employs the singularity swap quadrature (SSQ) method [1, 2, 10] in the azimuthal and (if needed) the polar direction, extending the applicability of the SSQ method to new kernels in 3D. At the highest level of the algorithm, error estimates from [42] ensure that S3Q is activated only when the regular quadrature fails to meet the desired accuracy. At the lowest level, newly derived quadrature and interpolation error estimates are used to adaptively subdivide the integration interval in the polar direction. While both types of estimates are important, the main innovation lies in the interpolation error estimation. Starting with the Hermite interpolation formula [44, Theorem 11.1] to express the error as a contour integral in the complex plane, the theoretical and computational framework in [3], previously applied solely to quadrature error estimation, is extended to also derive remarkably accurate interpolation error estimates.

The outline of this paper is as follows. In Section 2 we introduce our new quadrature method, detailing the “singularity swapping” technique used in both the azimuthal and polar directions, as well as the adaptive discretization scheme. Section 3 provides the necessary background and presents our new quadrature and interpolation error estimates for adaptive refinement. The computation of complex-valued roots of distance functions is detailed in Section 4. Section 5 examines the computational complexity of the proposed quadrature method, while Section 6 showcases numerical experiments that demonstrate its error control. Finally, we conclude in Section 7.

**2. The S3Q method.** In the previous section, we demonstrated the need for a special quadrature method for close evaluation of layer potentials. We now introduce our adaptive quadrature method, singularity swap surface quadrature (S3Q), designed to evaluate nearly singular layer potentials of the form (1.8) to controllable accuracy. We start by giving an overview of the method, before we discuss the details.

Given an error tolerance, we use a quadrature error estimate from [42] to determine whether regular quadrature provides insufficient accuracy. In such cases, we apply the S3Q method. First, we use interpolatory semi-analytical quadrature in the azimuthal direction, employing a singularity swap technique with an expansion in a Fourier basis [1]. This involves identifying the appropriate regularization (or “singularity swap”) for the integrand and analytically integrating the product of the Fourier basis functions and a simpler, nearly singular term through recurrence formulas. Assuming the layer density to be well resolved on the original grid<sup>2</sup>, the number of basis functions set by the grid will suffice. This is the case as the regularized factor depends only on the polar variable, as we will show.

Following this step, an integral along the polar direction remains. Since recurrence formulas were used in the prior evaluation, simple closed-form expressions for the integrands corresponding to each value of  $p$  are not available. For  $p > 1/2$ , the dominant behavior is nearly singular, albeit of lower degree compared to the original integrand. For  $p = 1/2$ , the integrand is nearly non-differentiable (nearly  $\mathcal{C}^0$ ), meaning its derivative is nearly singular<sup>3</sup>.

Nearly  $\mathcal{C}^0$  factors (and logarithmic near singularities that appear) for  $p = 1/2$  are efficiently integrated using regular quadrature on an adaptive grid, while stronger near singularities for  $p > 1/2$  can require semi-analytical quadrature. Our technique for integrating along the polar direction combines adaptivity with interpolatory semi-analytical quadrature in a Legendre polynomial basis. The adaptivity involves splitting the integration interval into segments, with a short segment centered around the nearly  $\mathcal{C}^0$  or nearly singular point, and recursively bisecting the remaining intervals as needed. Error estimates determine the appropriate lengths of these segments. The semi-analytical quadrature method, i.e. the singularity swap quadrature (SSQ) [2] used for  $p > 1/2$  requires the expansion of nearly  $\mathcal{C}^0$  functions, necessitating both quadrature and interpolation error estimates.

In Section 2.1, we describe how the layer potential is integrated in the azimuthal direction using SSQ. Section 2.2 analyzes the resulting integral in the polar direction, guiding the development of an SSQ method and the adaptive subdivision algorithm described in Section 2.3 and 2.4, respectively.

**2.1. Singularity swap quadrature in the azimuthal variable.** The SSQ method can be summarized in four steps: (1) find a pair of complex-valued roots of the distance function, (2) use these roots to “swap” the singularity to a simpler function with the same singularity locations, (3) expand all but the nearly singular part of the integrand in a new basis, and (4) evaluate the remaining nearly singular integrals involving the basis functions analytically. We refer to the later integrals as the basis integrals. We apply these steps to integrate our layer potential along the azimuthal direction. The results presented in this section extend the work in [1, 10] to three dimensions for axisymmetric surfaces. Our main analytical result of this section is provided in Theorem 2.6, which is established using two lemmas.

We seek to integrate (1.8) over the azimuthal variable  $\varphi$ . For ease of notation, we write

$$(2.1) \quad \mathcal{I}_\varphi(\theta) = \mathcal{I}_\varphi[\Theta_p](\theta, \mathbf{x}) = \int_0^{2\pi} \frac{f(\theta, \varphi)}{(R^2(\theta, \varphi, \mathbf{x}))^p} d\varphi.$$

<sup>2</sup>We say that a function is well resolved or well represented with  $n$  basis functions if the remaining basis coefficients are negligible and that a function is smooth if its basis coefficients decay rapidly, requiring only a small  $n$ .

<sup>3</sup>A nearly singular function is formally smooth, but has a peak with a large magnitude that is hard to resolve numerically. A nearly non-differentiable function does not grow large in magnitude but has high frequency content due to its nearly singular derivative.

In the discretized setting, we obtain an integral in  $\varphi$  for each discrete value of  $\theta$ .

Similar to [1], the singularity of (2.1) is swapped to a simpler function by multiplying and dividing by the periodic function  $|e^{i\varphi} - e^{i\varphi_0}|^{2p}$ . Here,  $\varphi_0 = \varphi_0(\theta, \mathbf{x})$  is the complex-valued root of  $R^2(\theta, \varphi, \mathbf{x})$  in the  $\varphi$  direction, which is analytically determined for axisymmetric surfaces using the formulas from [42], as stated in Lemma 2.1. The axial symmetry of the surface simplifies the regularized factor  $|e^{i\varphi} - e^{i\varphi_0}|^2/R^2(\theta, \varphi, \mathbf{x})$ , rendering it independent of  $\varphi$ . This result is given in Lemma 2.2 and proved in Appendix A.

LEMMA 2.1 (Root of  $R^2$  in  $\varphi$  [42]). *Let  $\gamma(\theta, \varphi)$  be parameterized as in (1.4) and  $R^2(\theta, \varphi, \mathbf{x})$  be defined according to (1.7). Consider a target point  $\mathbf{x} = (x, y, z) \in \mathbb{R}^3$  with  $\rho^2 = x^2 + y^2 > 0$  not on  $\gamma$ . Then, given  $\theta \in (0, \pi)$ ,  $R^2(\theta, \varphi, \mathbf{x}) = 0$  for  $\varphi = \varphi_0(\theta, \mathbf{x})$  with*

$$(2.2) \quad \varphi_0(\theta, \mathbf{x}) = \text{atan2}(y, z) \pm i \ln \left( \frac{\lambda(\theta) + \sqrt{\lambda(\theta)^2 - \rho^2 \sin^2(\theta)}}{\rho \sin(\theta)} \right), \quad \lambda(\theta) = \frac{\tilde{a}(\theta)^2 + \rho^2 + (\tilde{b}(\theta) - z)^2}{2a(\theta)},$$

where  $\tilde{a}(\theta) = a(\theta) \sin(\theta)$  and  $\tilde{b}(\theta) = b(\theta) \cos(\theta)$ . Here,  $\lambda(\theta) > \rho \sin(\theta)$  and  $\text{atan2}(\eta, \xi)$  is the argument of the complex number  $\xi + i\eta$ ,  $-\pi < \text{atan2}(\eta, \xi) \leq \pi$ .

LEMMA 2.2. *Assume the same notation and definitions as in Lemma 2.1. Let  $\varphi_0(\theta, \mathbf{x})$  and  $\lambda(\theta)$  be given by (2.2). Then, the regularized factor, equals*

$$(2.3) \quad \frac{|e^{i\varphi} - e^{i\varphi_0}|^2}{R^2(\theta, \varphi, \mathbf{x})} = \frac{1}{a(\theta)} \frac{1}{\lambda(\theta) + \sqrt{\lambda(\theta)^2 - \rho^2 \sin^2(\theta)}}.$$

We now have all the ingredients for Step 1-4 introduced above. Given a target point  $\mathbf{x}$ , to evaluate the integral (2.1) for each discrete  $\theta$ -value do:

**Step 1: Evaluate complex-valued root.** The complex-valued root in the  $\varphi$  direction of  $R^2(\theta, \varphi, \mathbf{x})$ , namely  $\varphi_0 = \varphi_0(\theta, \mathbf{x})$ , is evaluated according to (2.2).

**Step 2: Swap singularity.** Multiply and divide the integrand by the factor  $|e^{i\varphi} - e^{i\varphi_0}|^{2p}$ , and use Lemma 2.2 to simplify. Then (2.1) reads

$$(2.4) \quad \mathcal{I}_\varphi(\theta) = \frac{1}{a(\theta)^p} \frac{1}{\left( \lambda(\theta) + \sqrt{\lambda(\theta)^2 - \rho^2 \sin^2(\theta)} \right)^p} \underbrace{\int_0^{2\pi} \frac{f(\theta, \varphi)}{|e^{i\varphi} - e^{i\varphi_0}|^{2p}} d\varphi}_{=:\tilde{\mathcal{I}}_\varphi(\theta)}.$$

The  $\varphi$  dependence is now confined to the integral  $\tilde{\mathcal{I}}_\varphi$ , with the original numerator  $f(\theta, \varphi)$ , and a simpler denominator.

**Step 3: Expand in new basis.** Expand  $f(\theta, \varphi)$  in a Fourier basis. Given that  $f$  is smooth and known at equidistant nodes  $\{\varphi_\ell\}_{\ell=1}^{n_\varphi}$ , it is efficiently represented in terms of its Fourier series, which yields

$$(2.5) \quad \tilde{\mathcal{I}}_\varphi(\theta) = \sum_{k \in \mathbb{Z}} \hat{f}_k(\theta) \int_0^{2\pi} \frac{e^{ik\varphi}}{|e^{i\varphi} - e^{i\varphi_0}|^{2p}} d\varphi,$$

where  $\hat{f}_k$  denotes the Fourier coefficients of  $f$ . In practice,  $\hat{f}_k$  is computed by the fast Fourier transform (FFT) at an  $\mathcal{O}(n_\varphi \log(n_\varphi))$  cost for each  $\theta$ . An interpretation of (2.5) is that  $\tilde{\mathcal{I}}_\varphi(\theta)$  is computed using interpolatory quadrature on the unit circle, where the weights,

$$(2.6) \quad \int_0^{2\pi} \frac{e^{ik\varphi}}{|e^{i\varphi} - e^{i\varphi_0}|^{2p}} d\varphi, \quad k \in \mathbb{Z},$$

are the Fourier coefficients of  $|e^{i\varphi} - e^{i\varphi_0}|^{-2p}$ . A benefit of this approach is that the near singularity is contained within the Fourier basis integrals (2.6), which are independent of the layer density  $\sigma$ .

**Step 4: Analytically compute nearly singular basis integrals.** The final step is to evaluate the integrals (2.6) analytically. Introduce

$$(2.7) \quad r = e^{-|\operatorname{Im}(\varphi_0(\theta, \mathbf{x}))|},$$

where  $r \in \mathbb{R}$ ,  $0 < r < 1$ , implicitly depends on  $\theta$  and  $\mathbf{x}$ . Then,

$$(2.8) \quad \int_0^{2\pi} \frac{e^{ik\varphi}}{|e^{i\varphi} - e^{i\varphi_0}|^{2p}} d\varphi = 2e^{ik \operatorname{Re}(\varphi_0)} \underbrace{\int_0^\pi \frac{\cos(k\varphi)}{(1 - 2r \cos(\varphi) + r^2)^p} d\varphi}_{=:\omega_k^p(r)},$$

The function  $\omega_k^p(r)$  is computed for  $k = 0, 1, 2, \dots, k_{\max}$  (note that  $\omega_{-k}^p = \omega_k^p$ ) using the analytical recurrence formulas provided in Lemma 2.3. These calculations involve the complete elliptic integrals of the first and second kind, defined as

$$(2.9) \quad K(k^2) = \int_0^{\pi/2} \frac{d\theta}{\sqrt{1 - k^2 \sin^2(\theta)}} \quad \text{and} \quad E(k^2) = \int_0^{\pi/2} \sqrt{1 - k^2 \sin^2(\theta)} d\theta,$$

respectively. The proof of Lemma 2.3 is presented in Appendix A.

LEMMA 2.3. *Let  $k \in \mathbb{N}_0$ ,  $p = \bar{p} + 1/2$ ,  $\bar{p} \in \mathbb{Z}^+$ , and  $\alpha \in \mathbb{R}$ , where  $0 < \alpha < 1$ . The complete elliptic integral of the first kind,  $K(\alpha^2)$ , and of the second kind,  $E(\alpha^2)$ , are defined by (2.9). Then,*

$$(2.10) \quad \omega_k^p(\alpha) = \int_0^\pi \frac{\cos(k\varphi)}{(1 - 2\alpha \cos(\varphi) + \alpha^2)^p} d\varphi$$

is given by

$$(2.11) \quad \omega_k^p(\alpha) = \frac{1}{(1 - \alpha)^{2p-1}} \mu_k^p(\alpha),$$

where

$$(2.12) \quad \mu_k^p(\alpha) = \begin{cases} \frac{1 + \alpha^2}{\alpha} \frac{2(k-1)}{2k-1} \mu_{k-1}^p(\alpha) - \frac{2k-3}{2k-1} \mu_{k-2}^p(\alpha), & p = 1/2 \text{ and } k = 2, 3, \dots, \\ \frac{1 + \alpha^2}{2\alpha} \mu_{k-1}^p(\alpha) - \frac{(1-\alpha)^2}{2\alpha} \frac{p+k-2}{p-1} \mu_{k-1}^{p-1}(\alpha), & p > 1/2 \text{ and } k = 1, 2, \dots \end{cases}$$

The initial values for  $\mu_k^p(\alpha)$  for  $p = 1/2, 3/2, 5/2$  are

$$(2.13) \quad \mu_0^{1/2}(\alpha) = 2K(\alpha^2), \quad \mu_1^{1/2}(\alpha) = \frac{2}{\alpha} (K(\alpha^2) - E(\alpha^2)),$$

$$(2.14) \quad \mu_0^{3/2}(\alpha) = \frac{2}{1+\alpha} \left( \frac{2}{1+\alpha} E(\alpha^2) - (1-\alpha)K(\alpha^2) \right),$$

$$(2.15) \quad \mu_0^{5/2}(\alpha) = \frac{2}{3(1+\alpha)^4} (8(1+\alpha^2)E(\alpha^2) - (1-\alpha)(1+\alpha)(5+3\alpha^2)K(\alpha^2)).$$

Remark 2.4. It turns out that  $\omega_k^p(\alpha) = (2/\pi)b_p^{(k)}(\alpha)$ , where  $b_p^{(k)}$  are the so-called Laplace coefficients, which e.g. appear in multipole expansions of various potentials. For example, consider two points  $\mathbf{r} = (r, \theta, \varphi)$  and  $\mathbf{r}' = (r', \theta', \varphi')$  in spherical coordinates. Let  $h = r'/r$  and  $\psi$  denote the angle between the two vectors. Then the potential

$$(2.16) \quad \frac{1}{|\mathbf{r} - \mathbf{r}'|^{2p}} = \frac{1}{r^{2p}} \frac{1}{(1 - 2h \cos(\psi) + h^2)^p}$$

can be expanded as

$$(2.17) \quad \frac{1}{(1 - 2h \cos(\psi) + h^2)^p} = \frac{1}{2} b_p^{(0)}(h) + \sum_{k=1}^{\infty} b_p^{(k)}(h) \cos(k\psi).$$

Laplace's study of the integrals  $b_p^{(k)}$ , in the context of celestial mechanics, dates back to 1785 [34], where similar, and numerically comparable, recurrence formulas to those presented in Lemma 2.3 are provided. However, due to their inaccessibility and lack of proof, we still use and find value in presenting the ones we derived for this work.

*Remark 2.5* (Accuracy and stability of recurrence formulas for  $\mu_k^p$ ). The recurrence relations for  $\mu_k^p(\alpha)$  in (2.12) can exhibit a highly unstable numerical behavior. The solution to the recurrence relation (i.e.  $\mu_k^p(\alpha)$ ) tend to zero as the number of forward steps  $k \rightarrow \infty$ , with a rate that increases the closer the argument  $\alpha$  is to zero. However, for arbitrary initial values, the solution to the homogeneous three-term recurrence relation grows exponentially in magnitude with  $k$ . After a number of forward recursion steps, the desired vanishing solution can potentially be obscured by the exponentially increasing component, readily introduced by roundoff errors, particularly for large  $k$ . To mitigate this, we use an error estimate to assess whether the forward recursions in (2.12) introduce errors larger than the error tolerance. If they do, we abandon these formulas in favor of the numerically stable method described in [7]. In short, the recurrence relation is rewritten as an inhomogeneous tridiagonal matrix equation of size  $k_0 - 1$ , where its solution is forced to vanish at  $k = k_0$ . This procedure can be viewed as solving a one-dimensional boundary value problem, where one of the boundary values is set to the initial value of the recurrence relation, and the other to zero. Further details on this stabilization process are provided in Appendix B.

With the four steps of the SSQ method complete, we now present our main analytical result of this section that gives a formula for the layer potential in (1.3) as a one-dimensional integral. The proof is presented in Appendix A.

**THEOREM 2.6.** *Let  $\gamma : \{(\theta, \varphi) \in [0, \pi] \times [0, 2\pi)\} \rightarrow \mathbb{R}^3$  be a smooth axisymmetric surface parameterized as*

$$(2.18) \quad \gamma(\theta, \varphi) = (a(\theta) \sin(\theta) \cos(\varphi), a(\theta) \sin(\theta) \sin(\varphi), b(\theta) \cos(\theta)),$$

where  $a(\theta), b(\theta) > 0$ . Consider the layer potential

$$(2.19) \quad u(\mathbf{x}) = \iint_{\gamma} \frac{f(\theta, \varphi)}{\|\gamma(\theta, \varphi) - \mathbf{x}\|^{2p}} d\varphi d\theta,$$

where  $2p \in \mathbb{Z}^+$  for a target point  $\mathbf{x} = (x, y, z) \in \mathbb{R}^3$  not on  $\gamma$  with  $\rho = \sqrt{x^2 + y^2}$ . Let  $\varphi_0$  and  $\lambda$  be defined according to (2.2), i.e. so that  $R^2(\theta, \varphi_0(\theta, \mathbf{x}), \mathbf{x}) = R^2(\theta, \overline{\varphi_0}(\theta, \mathbf{x}), \mathbf{x}) = 0$  where  $R^2(\theta, \varphi, \mathbf{x})$  is defined by (1.7). Let  $r(\theta) = e^{-|\text{Im}(\varphi_0(\theta, \mathbf{x}))|}$ , and  $\mu_k^p$  be defined by (2.10)-(2.11).

Then, the layer potential (2.19) can be expressed as

$$(2.20) \quad u(\mathbf{x}) = \int_0^\pi \frac{1}{\sqrt{a(\theta)}} \frac{1}{\left(\lambda(\theta) + \sqrt{\lambda(\theta)^2 - \rho^2 \sin^2(\theta)}\right)^{1/2}} \frac{1}{(R_\lambda^2(\theta, \mathbf{x}))^{p-1/2}} \mathcal{F}(\theta) d\theta,$$

where

$$(2.21) \quad \mathcal{F}(\theta) = 2 \sum_{k \in \mathbb{Z}} \hat{f}_k(\theta) e^{ik \text{Re}(\varphi_0(\theta, \mathbf{x}))} \mu_k^p(r(\theta)).$$

Here,  $\hat{f}_k(\theta)$  denotes the azimuthal Fourier coefficients of  $f(\theta, \varphi)$  in (2.19), and the squared distance function  $R_\lambda^2$  is defined as

$$(2.22) \quad R_\lambda^2(\theta, \mathbf{x}) = (a(\theta) \sin(\theta) - \rho)^2 + (b(\theta) \cos(\theta) - z)^2.$$

The result we just obtained is exact due to the non-truncated Fourier series in (2.5), leading to (2.21). The Fourier sum  $\mathcal{F}$  in (2.21), equals

$$(2.23) \quad \mathcal{F}(\theta) = (1 - r(\theta))^{2p-1} \tilde{\mathcal{I}}_\varphi(\theta),$$

with  $\tilde{\mathcal{I}}_\varphi(\theta)$  defined in (2.4). This sum is in practice truncated at some maximum wavenumber  $k_{\max} \leq (n_\varphi - 1)/2$ , assuming  $n_\varphi$  odd. This truncation introduces an error that is negligible if  $f(\theta, \varphi)$  is well resolved on the azimuthal grid.

In essence, Theorem 2.6 reveals that after integrating over the azimuthal direction, the dominant behavior is nearly  $\mathcal{C}^0$  and logarithmically nearly singular for  $p = 1/2$ , while for  $p > 1/2$  it is nearly singular. Importantly, the power  $p$  in the two left-most functions of (2.4) is reduced to  $1/2$  in (2.20), regardless of  $p$ , as can be seen in the proof in Appendix A. In the next section, we study the integrand's behavior in greater detail to determine how (2.20) should be best evaluated.

**2.2. Analysis of integral in the polar direction.** Here we analyze the integrand in (2.20), which remains after the layer potential has been integrated in the azimuthal direction, to determine the best approach for its evaluation.

We write (2.20) as

$$(2.24) \quad u(\mathbf{x}) = \int_0^\pi \frac{1}{\sqrt{a(\theta)}} \Lambda^{\text{sq}}(\theta, \mathbf{x}) \mathcal{F}(\theta, p, \mathbf{x}) (R_\lambda^2(\theta, \mathbf{x}))^{-(p-1/2)} d\theta,$$

where

$$(2.25) \quad \Lambda^{\text{sq}}(\theta, \mathbf{x}) = \left( \lambda(\theta) + \sqrt{\lambda(\theta)^2 - \rho^2 \sin^2(\theta)} \right)^{-1/2},$$

with  $\lambda$  defined in (2.2). The function  $\mathcal{F}$  is written with three arguments to emphasize its dependencies.

Among the factors of the integrand, the inverse  $R_\lambda^2$  function is the most difficult to resolve, as it has a nearly singular behavior. Note, however, that its power is lower compared to the original  $R^2$  function, and that this factor evaluates to 1 when  $p = 1/2$ . The function  $\mathcal{F}(\theta, p, \mathbf{x})$ , defined via recurrence relations, may have a logarithmic near singularity, see Remark 2.7. The factor  $\Lambda^{\text{sq}}(\theta, \mathbf{x})$  has a nearly singular derivative, and, while not growing in magnitude, is still difficult to resolve numerically. The factor  $1/\sqrt{a(\theta)}$  is benign.

Figure 2.1 illustrates the typical behavior of the functions in (2.24) for the close evaluation of the layer potential (1.3) defined on a spheroidal surface with  $p = 1/2$  and  $p = 3/2$ . Each function is represented in a Chebyshev series, and the decay of the magnitudes of the Chebyshev coefficients is observed. We observe that  $\Lambda^{\text{sq}}(\theta, \mathbf{x})$  and  $\mathcal{F}(\theta, p, \mathbf{x})$  require similar polynomial degrees to be fully resolved. In contrast,  $(R_\lambda^2(\theta, \mathbf{x}))^{-(p-1/2)}$ , for  $p > 1/2$ , requires significantly higher degrees. The function  $(R_\lambda^2(\theta, \mathbf{x}))^{-(p-1/2)}$ , for  $p > 1/2$ , has a singularity at  $\theta_0^\lambda \in \mathbb{C}$ , a root of  $R_\lambda^2$ . This singularity can be regularized by  $|\theta - \theta_0^\lambda|^{2p-1}$ . As can be seen in Figure 2.1d,  $(R_\lambda^2(\theta, \mathbf{x}))^{-(p-1/2)}$  requires around  $6.5 \cdot 10^4$  terms to be fully resolved, whereas the regularized function  $|\theta - \theta_0^\lambda|^{2p-1} (R_\lambda^2(\theta, \mathbf{x}))^{-(p-1/2)}$  needs remarkably few terms.

The function  $\Lambda^{\text{sq}}(\theta, \mathbf{x})$  has branch points at  $\{\theta_0^\lambda, \overline{\theta_0^\lambda}\}$ . While it may be possible to develop a SSQ method for the product  $\Lambda^{\text{sq}}(\theta, \mathbf{x}) (R_\lambda^2(\theta, \mathbf{x}))^{-(p-1/2)}$ , the behavior of  $\mathcal{F}(\theta, p, \mathbf{x})$  suggests that no significant advantage would be gained from such a method over one designed solely for  $R_\lambda^2$ .

In summary, an adaptive subdivision of the integration interval will be employed, using an SSQ method for the  $R_\lambda^2$  function when present, i.e. for  $p > 1/2$ . For  $p = 1/2$ , Gauss–Legendre quadrature will instead be applied over each subinterval. Details on this adaptive discretization are provided in Section 2.4. We now describe the special quadrature method we construct for  $p > 1/2$ .

*Remark 2.7* (The function  $\mathcal{F}$ ). The function  $\mathcal{F}$  is given by (2.21), with  $\mu_k^p$  defined via recurrence formulas (2.12). The initial values (2.13)–(2.15) include the complete elliptic integral of the first kind  $K(r^2)$ . As the evaluation point  $\mathbf{x}$  approaches the surface,  $r(\theta) = e^{-|\text{Im}(\varphi_0(\theta, \mathbf{x}))|} \rightarrow 1^-$ , causing  $K(r^2)$  to diverge logarithmically. Consequently,  $\mathcal{F}$  typically contains a nearly logarithmic singularity, although a complete singularity characterization has not yet been achieved that enables a simple singularity swap.

**2.3. Singularity swap quadrature in the polar variable.** To evaluate the integral (2.20) for  $p > 1/2$  on a subinterval  $[\theta_a, \theta_b] \subseteq [0, \pi]$ , we follow the same steps as in the azimuthal direction in Section 2.1. This involves finding the root of the corresponding squared distance function, swapping the singularity to a simpler function, expanding all terms but the nearly singular component in a new basis, and lastly analytically evaluating the resulting nearly singular basis integrals.



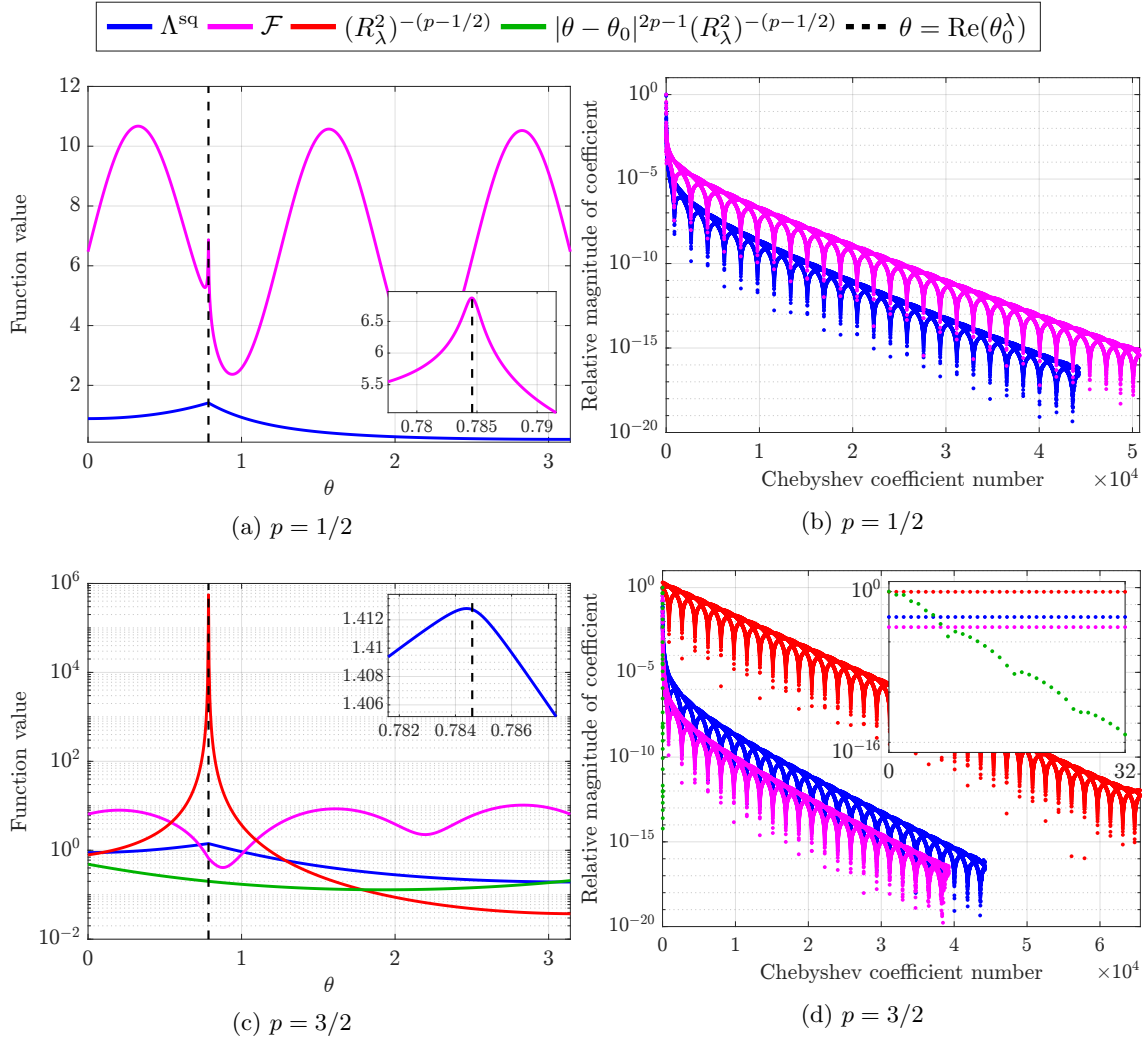


Fig. 2.1: Typical behavior of the functions appearing in the integrand of (2.24). In panels (a) and (c) the functions are shown and  $\theta = \text{Re}(\theta_0^\lambda)$ , for this specific target point, is marked. Panels (b) and (d) show the relative decay of their Chebyshev coefficients. The quantity  $|\theta - \theta_0|^{2p-1} (R_\lambda^2)^{-(p-1/2)}$  is plotted in green in panel (c), with the decay of its Chebyshev coefficients in panel (d) showing its low frequency content. Here,  $\theta_0^\lambda$  is a root of  $R_\lambda^2$  defined by (4.10) and (2.22), respectively. In this example,  $k(\mathbf{x}, \mathbf{y}) = 1$  and  $\sigma(\gamma(\theta, \varphi)) = \sin(5\theta)e^{-\cos^2(\varphi)} + 1.03$ .

Given that  $R_\lambda^2(\theta, \mathbf{x})$  is real for real  $\theta$ , its roots come in complex conjugate pairs. For spheroidal surfaces, we find these roots analytically. For general axisymmetric surfaces, we perform a one-dimensional root-finding procedure. See Section 4 for more details. If the curve we are integrating along is not too curved and  $\mathbf{x}$  is close to it, there will typically only be one nearby pair of roots [2]. Let  $\{\theta_0^\lambda(\mathbf{x}), \overline{\theta_0^\lambda(\mathbf{x})}\} = \{\theta(t_0^\lambda(\mathbf{x}), \theta_a, \theta_b), \theta(\overline{t_0^\lambda(\mathbf{x})}, \theta_a, \theta_b)\}$  denote the pair of roots of  $R_\lambda^2$  closest to the interval  $[\theta_a, \theta_b]$ , where the linear map  $\theta(t, \theta_a, \theta_b)$  is defined in (1.5). For brevity, the dependence on  $\mathbf{x}$  will be omitted for the complex-valued roots throughout the remainder of Section 2.

Following af Klinteberg & Barnett [2], we define

$$(2.26) \quad H(\theta) := \frac{1}{\sqrt{a(\theta)}} \Lambda^{\text{sq}}(\theta, \mathbf{x}) \mathcal{F}(\theta, p, \mathbf{x}) \frac{|\theta - \theta_0^\lambda|^{2p-1}}{(R_\lambda^2(\theta, \mathbf{x}))^{p-1/2}}$$

allowing us to write (2.24) on  $[\theta_a, \theta_b]$  as

$$(2.27) \quad u(\mathbf{x}) = \theta_{\text{sc}}^{2(1-p)} \int_{-1}^1 \frac{H(\theta(t, \theta_a, \theta_b))}{|t - t_0^\lambda|^{2p-1}} dt,$$

where we used that  $|\theta - \theta_0^\lambda| = \theta_{\text{sc}}|t - t_0^\lambda|$ . The singularity swap has transformed the integral on the curve in the polar direction to a denominator that corresponds to that of a straight line.

The next step is to expand  $H$  in a real monomial basis,

$$(2.28) \quad H(\theta(t, \theta_a, \theta_b)) \approx \sum_{k=1}^{n_t} c_k t^{k-1},$$

where the coefficients  $c_k$  can be found by solving the Vandermonde system (see Remark 2.10 for more details)

$$(2.29) \quad \mathbf{A} \mathbf{c} = \mathbf{h}.$$

Here,  $\mathbf{A} \in \mathbb{R}^{n_t \times n_t}$  is the Vandermonde matrix and  $\mathbf{h} \in \mathbb{R}^{n_t}$  contains the elements  $\{H(\theta(t_i, \theta_a, \theta_b))\}_{i=1}^{n_t}$ , with  $t_i$  being the Gauss–Legendre quadrature nodes. Analogously to (2.5), we obtain

$$(2.30) \quad u(\mathbf{x}) \approx \theta_{\text{sc}}^{2(1-p)} \sum_{k=1}^{n_t} c_k \nu_k^p(t_0^\lambda) = \theta_{\text{sc}}^{2(1-p)} \mathbf{c}^T \boldsymbol{\nu}^p,$$

where  $\boldsymbol{\nu}^p \in \mathbb{R}^{n_t}$  denotes the vector with entries given by

$$(2.31) \quad \nu_k^p(t_0^\lambda) = \int_{-1}^1 \frac{t^{k-1}}{|t - t_0^\lambda|^{2p-1}} dt, \quad k = 1, \dots, n_t,$$

which can be efficiently evaluated using the recurrence formulas provided in Lemma 2.8. The proof is presented in Appendix A. The superscript  $T$  in (2.30) indicates non-conjugate transpose.

The error of the presented quadrature method for  $p > 1/2$  essentially comes from how well  $H$  is represented in the new basis. That is, the error in (2.30) is largely due to the best polynomial representation (2.28). While the singularity swap in (2.26) regularized the singular behavior of  $(R_\lambda^2)^{-(p-1/2)}$ , the region of analyticity of  $H$  remains limited by the roots of  $\Lambda^{\text{sq}}$ ,  $\{\theta_0^\lambda(\mathbf{x}), \overline{\theta_0^\lambda(\mathbf{x})}\}$ . Hence, for close evaluation points, the coefficients  $c_k$  in (2.28) decay slowly with  $n_t$  for close evaluations.

To address this, the interval  $[0, \pi]$  in  $\theta$  is subdivided into multiple Gauss–Legendre panels to ensure that the roots after being remapped to  $[-1, 1]$  are sufficiently far from the interval. This increases the decay rate of the coefficients and enhances the accuracy of the approximation. The same refinement strategy is required for  $p = 1/2$ , where regular Gauss–Legendre quadrature is used. The following section describes how this discretization refinement is realized adaptively.

LEMMA 2.8. *Let  $k \in \mathbb{N}$ ,  $p = \bar{p} + 3/2$ ,  $\bar{p} \in \mathbb{Z}^+$ , and  $t_0^\lambda = t_r + it_i$ , where  $t_r, t_i \in \mathbb{R}$  and  $t_0^\lambda \notin [-1, 1]$ . Then, the integrals*

$$(2.32) \quad \nu_k^p(t_0^\lambda) = \int_{-1}^1 \frac{t^{k-1}}{|t - t_0^\lambda|^{2p-1}} dt$$

can be expressed as

$$(2.33) \quad \nu_k^p(t_0^\lambda) = \begin{cases} \frac{1 - (-1)^{k-2}}{k-2} + 2t_r \nu_{k-1}^p(t_0^\lambda) - |t_0^\lambda|^2 \nu_{k-2}^p, & p = 3/2 \text{ and } k \geq 3, \\ \nu_{k-2}^{p-1}(t_0^\lambda) + 2t_r \nu_{k-1}^p(t_0^\lambda) - |t_0^\lambda|^2 \nu_{k-2}^p(t_0^\lambda), & p > 3/2 \text{ and } k \geq 3. \end{cases}$$

Moreover, if  $t_r = 0$ , then  $\nu_k^p(t_0^\lambda) = 0$  for  $k \in 2\mathbb{N}$ . The expressions for the initial values for  $\nu_k^p(t_0^\lambda)$  for  $p = 3/2, 5/2$  are found in (A.25)–(A.28) in Appendix A.

*Remark 2.9* (Stability and accuracy of recurrence formulas  $\nu_k^p$ ). If  $|t_0^\lambda| > 1$ , which can occur when  $\mathbf{x}$  is far from Gauss–Legendre panel under consideration, errors due to finite precision can be greatly amplified in the forward recurrences (2.33). Additionally, inaccuracies arise if  $t_0^\lambda$  lies within in one of the two cones extending outwards from the endpoints  $\pm 1$ , which also was noted by [2]. However, by construction of the adaptive refinement scheme in Section 2.4, such problematic cases are rare. Notably, for  $|t_0^\lambda| \leq 1.1$  and  $n_t$  not too large, the forward recurrence errors typically remain small. For  $|t_0^\lambda| > 1.1$ , we run the recurrences backwards, assuming that the last two terms can be computed accurately via regular quadrature. We use an error estimate from [3] to determine this. If the estimate indicates a high quadrature error, we revert to the forward recurrence.

*Remark 2.10* (Arbitrary function interpolation and stability). Equation (2.30) approximates the layer potential for a given function  $H$ . The function  $H$  is sampled at the Gauss–Legendre nodes to produce  $\mathbf{h}$ . Instead of solving (2.29) for the coefficient vector  $\mathbf{c}$ , an alternative system can be solved instead, as shown in [29]. Substituting (2.29) into (2.30) and disregarding the factor  $\theta_{\text{sc}}^{2(1-p)}$  for simplicity gives

$$(2.34) \quad u(\mathbf{x}) \approx \mathbf{c}^T \boldsymbol{\nu}^p = (\mathbf{A}^{-1} \mathbf{h})^T \boldsymbol{\nu}^p = \mathbf{h}^T (\mathbf{A}^{-1})^T \boldsymbol{\nu}^p = \mathbf{h}^T \boldsymbol{\xi}^p = (\boldsymbol{\xi}^p)^T \mathbf{h},$$

where  $\boldsymbol{\xi}^p$  is the solution to a different Vandermonde system,

$$(2.35) \quad \mathbf{A}^T \boldsymbol{\xi}^p = \boldsymbol{\nu}^p.$$

This system, unlike (2.29), is independent of  $\mathbf{h}$ . While solving this system might appear challenging due to the exponential growth of the Vandermonde matrix’s condition number with increasing  $n_t$  [25], [29] points out that if the underlying function is well resolved, this ill-conditioning does not affect the interpolation performance, at least up to  $n_t = 40$ . These Vandermonde systems can be solved at an  $\mathcal{O}(n_t^2)$  cost using either the Björck–Pereyra algorithm [15] or through a precomputed LU factorization of  $\mathbf{A}$ .

**2.4. Local refinement scheme.** To efficiently represent the integrand or its factors in (2.20) using a monomial basis, we adopt a local refinement strategy in the polar direction based on panel subdivision, as proposed by Fryklund et al. [24].

The integration strategy along the polar direction is dictated by how well the functions  $\Lambda^{\text{sq}}$  and  $\mathcal{F}$  defined by (2.25) and (2.21), respectively, can be represented by a Lagrange polynomial. By splitting the  $t$  interval into several segments, remapping each to  $[-1, 1]$ , the approximation power is enhanced. As shown in Figure 2.1,  $\Lambda^{\text{sq}}$  and  $\mathcal{F}$  are typically challenging to resolve only in a small region around  $\text{Re}(t_0^\lambda(\mathbf{x}))$ , making adaptive refinement around this region efficient.

Given a panel  $\Gamma \in [-1, 1]$  where both the geometry and layer density are well resolved, and a target point  $\mathbf{x}$  with corresponding root  $t_0^\lambda$  of  $R_\lambda^2$ , we subdivide  $\Gamma$  into  $n_{\text{pan}}$  number of  $n_{\text{GL}}$ -point subpanels defined on  $[t_a^i, t_b^i]$ ,  $i = 1, \dots, n_{\text{pan}}$ . The process begins with centering a panel with length  $\Delta t_{\text{max}}$  around  $\text{Re}(t_0^\lambda)$ <sup>4</sup> and then recursively bisecting each subinterval next to it, as illustrated in Figure 2.2. This subdivision is designed to satisfy

$$(2.36) \quad \mathbb{E}(n_{\text{GL}}, t_a^i, t_b^i, p, \sigma, \mathbf{x}) \leq \epsilon_i, \quad i = 1, \dots, n_{\text{pan}},$$

where  $\mathbb{E}(n_{\text{GL}}, t_a, t_b, p, \sigma, \mathbf{x})$  denotes the error estimate for a general  $n_{\text{GL}}$ -point Gauss–Legendre panel on  $[t_a, t_b]$  to be discussed in Section 3, and  $\sum_{i=1}^{n_{\text{pan}}} \epsilon_i = \epsilon$ , with  $\epsilon$  being the desired error tolerance. Before the recursive bisection, the centered panel length  $\Delta t_c$  is set to be as large as possible while still ensuring  $\Delta t_c \leq \Delta t_{\text{max}}$  and that it falls within  $[-1, 1]$ , i.e.,

$$(2.37) \quad \Delta t_c = \min(\Delta t_{\text{edge}}, \Delta t_{\text{max}}),$$

with

$$(2.38) \quad \Delta t_{\text{edge}} = 2(1 - |\text{Re}(t_0^\lambda)|).$$

<sup>4</sup>In the local coordinates of the centered panel,  $t_0^\lambda$  will be purely imaginary, ensuring stability of the recurrence formulas in (2.33).

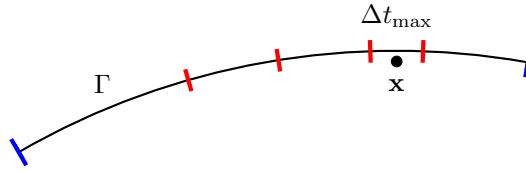


Fig. 2.2: Illustration of an adaptive panel subdivision, showing the short centered interval and the recursively subdivided intervals next to it.

In practice, we find  $\Delta t_{\max}$  using the secant method with step size control, see Appendix C for more details.

The output of the algorithm is a subdivision of  $[-1, 1]$  into  $n_{\text{pan}}$   $n_{\text{GL}}$ -point Gauss–Legendre panels that allow the layer potential (2.24) to be evaluated with accuracy  $\epsilon$ . Specifically, we interpolate the layer density data from the quadrature nodes on  $\Gamma$  to the nodes on the subpanels via barycentric Lagrange interpolation [14], evaluate the layer potential in  $\mathbf{x}$  on the subpanels, and sum each contribution. To implement this refinement strategy, we need to concretize the error estimate  $E$  in (2.36), which is the topic of the following section.

**3. Error analysis and estimates.** In Section 3.1, we introduce a general framework for understanding quadrature and interpolation errors using contour integrals in the complex plane, highlighting how the singularities of the function being integrated or interpolated influence these errors. Based on [42, 3], Section 3.2 briefly reviews how it is used to derive quadrature error estimates for generic layer potentials of the form (1.1). This framework also aids in the derivations of new quadrature and interpolation error estimates in Sections 3.3–3.4, which are essential for the adaptive panel subdivision outlined in Section 2.4.

**3.1. Quadrature and interpolation error formulas using complex analysis.** Consider the integral of a function  $g$  defined over a base interval  $E \subset \mathbb{R}$ ,

$$(3.1) \quad \mathcal{I}[g] = \int_E g(t) dt,$$

approximated by an  $n$ -point quadrature rule with quadrature nodes  $\{t_\ell\}_{\ell=1}^n$  and corresponding weights  $\{w_\ell\}_{\ell=1}^n$ ,

$$(3.2) \quad \mathcal{Q}_n[g] = \sum_{\ell=1}^n g(t_\ell)w_\ell.$$

The quadrature error is then given by

$$(3.3) \quad E_n[g] = \mathcal{I}[g] - \mathcal{Q}_n[g].$$

The rate at which  $E_n[g]$  decay as  $n$  increases depends on the smoothness of  $g$  and the chosen quadrature rule.

Classical estimates of (3.3) for the Gauss–Legendre rule typically involve high-order derivatives of  $g$ . These estimates are therefore only practical for very smooth integrands and tend to overestimate the error when  $g$  has singularities near  $E$ . In such nearly singular cases, these traditional estimates can even incorrectly suggest an increase in error as  $n$  grows, despite the actual error decreasing [5].

More reliable in these situations is an approach based on complex analysis, as described by Donaldson & Elliot [21]. They express the error as a contour integral in the complex plane,

$$(3.4) \quad E_n[g] = \frac{1}{2\pi i} \int_C g(t)k_n(t) dt,$$

where the contour  $C$  in Figure 3.1, containing the integration interval  $E$ , is chosen so that the complex continuation of  $g$  is analytic on and inside  $C$ . The error (or remainder) function  $k_n(t)$  depends on the quadrature rule and is detailed in Section 3.3.2 for the Gauss–Legendre quadrature rule.

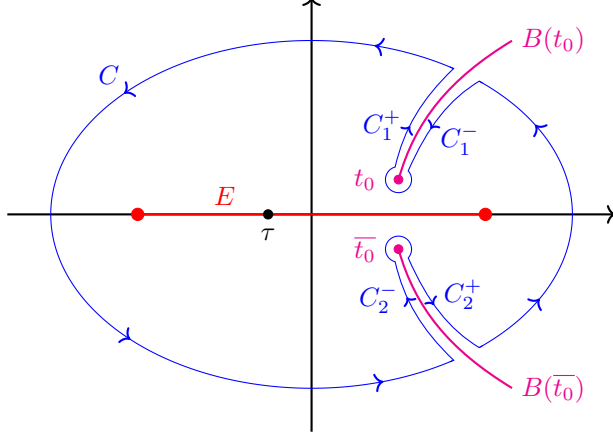


Fig. 3.1: Sketch of the contour  $C$ , the base interval  $E$ , interpolation point  $\tau$ , and the deformations  $C_1 = C_1^- \cup C_1^+$  and  $C_2 = C_2^- \cup C_2^+$  circumventing the singularities  $t_0$  and  $\bar{t}_0$  with branch cuts  $B(t_0)$  and  $B(\bar{t}_0)$ , respectively.

A central technique in deriving estimates of (3.4), introduced in [23], involves deforming the contour  $C$  away from  $E$  while avoiding all singularities. Assuming the integrand tends to zero faster than  $|t|^{-1}$  as  $|t| \rightarrow \infty$ , contributions from parts of  $C$  far from  $E$  vanish. Thus,  $C$  can be extended to infinity, leaving only the contribution from the singularities and their branch cuts. The particular choice of branch cuts in [23] is essential for obtaining accurate, simplified analytical estimates. For integrands with multiple pairs of complex conjugate singularities, such as (1.1), all pairs contribute to the error, but typically only the pair closest to  $E$  has a significant contribution, and the others can safely be discarded [3, 2]. The functions considered in this work have branch point singularities, meaning the main error contribution comes from a neighborhood around these branch points and their branch cuts, illustrated in Figure 3.1.

For an arbitrary function  $g$  and  $n$  distinct sample points  $\{t_k\}_{k=1}^n$  on  $E$ , then there exists a unique polynomial  $p_{n-1}$  of degree at most  $n-1$  such that  $p(t_k) = g(t_k)$ ,  $k = 1, \dots, n$ . This polynomial can be represented in various ways, but due to its superior stability and efficiency, we construct it using the barycentric Lagrange interpolation formula [14, 44]

$$(3.5) \quad p_{n-1}(t) = \ell_n(t) \sum_{k=1}^n \frac{w_k g(t_k)}{t - t_k},$$

with the barycentric weights  $\{w_k\}_{k=1}^n$

$$(3.6) \quad w_k = \frac{1}{\ell'_n(t_k)} = \left( \prod_{j=1, j \neq k}^n (t_k - t_j) \right)^{-1},$$

where the node polynomial is defined as

$$(3.7) \quad \ell_n(t) = \prod_{k=1}^n (t - t_k).$$

The polynomial interpolation error at  $\tau \in E$  is

$$(3.8) \quad E_n^I[g](\tau) = g(\tau) - p_{n-1}(\tau),$$

which, by the Hermite interpolation formula [44, Theorem 11.1], can be expressed as a contour integral in the complex plane,

$$(3.9) \quad E_n^I[g](\tau) = \frac{1}{2\pi i} \int_C \frac{\ell_n(\tau)}{\ell_n(t)} \frac{g(t)}{t - \tau} dt.$$

This formula holds under the same assumptions as stated below (3.4), namely that  $g$  is analytic on and inside  $C$ , and that  $E$  is contained within  $C$ . We are interested in the maximum absolute interpolation error of  $g$  on  $E$ ,

$$(3.10) \quad |E_n^I[g]| = \max_{\tau \in E} |E_n^I[g](\tau)|.$$

Comparing (3.9) with (3.4), we see that, instead of the error function  $k_n(t)$  that depends on the quadrature rule, we have the factor  $\ell_n(\tau)/(\ell_n(t)(t-\tau))$ , which depends on the node distribution and  $\tau \in E$ . This factor shares the important property with  $k_n(t)$  that it vanishes far from  $E$ .

**3.2. Quadrature error estimates for surfaces in  $\mathbb{R}^3$ .** Consider the parametrization  $\gamma(t, \varphi)$  for  $t \in [-1, 1]$ , representing the pullback of the axisymmetric surface  $\gamma(\theta(t, \theta_a, \theta_b), \varphi)$  as defined in (1.4). The functions  $f(t, \varphi)$  and  $R^2(t, \varphi, \mathbf{x})$  are defined analogously. Similar to (1.8), the layer potential can be written as

$$(3.11) \quad \int_{-1}^1 \int_0^{2\pi} \Theta_p(t, \varphi) \, d\varphi \, dt, \quad \Theta_p(t, \varphi) = \frac{f(t, \varphi)}{(R^2(t, \varphi, \mathbf{x}))^p},$$

where  $\mathbf{x} \in \mathbb{R}^3$  is the target point. The function  $f$  is assumed to be a smooth, and for simplicity, we omit the scaling factor associated with the linear map from  $t$  to  $\theta$ .

Using the notation from Section 1.1, the quadrature error for (3.11) can be approximated as [3],

$$(3.12) \quad E_{n_t, n_\varphi}^2 \Theta_p \approx (\mathcal{I}_t E_{\varphi, n_\varphi} + \mathcal{I}_\varphi E_{t, n_t}) \Theta_p,$$

where, for simplicity, brackets used in previous sections are omitted here; for instance,  $\mathcal{I}_{t, n_t} \Theta_p$  means the integration of  $\Theta_p$ , evaluated at  $\mathbf{x}$ , in the  $t$  direction using an  $n_t$ -point quadrature rule. Essentially, (3.12) suggests that the regular quadrature error over the surface can be approximated by first estimating the quadrature error along one direction and then integrating it along the other direction.

Consider the error associated with integrating (3.11) in the  $t$  direction over the base interval  $E = [-1, 1]$  using an  $n_t$ -point quadrature rule for a fixed value of  $\varphi$ , denoted by  $E_{t, n_t} \Theta_p$ . By (3.4),  $E_{t, n_t} \Theta_p$  can be expressed as a contour integral over the contour  $C$  depicted in Figure 3.1. Since  $p$  is half-integer, the singularities of the integrand, located at the roots of  $R^2(t, \varphi, \mathbf{x})$  in  $t$ , are branch point singularities. As motivated in Section 3.1, we focus only on the pair of roots closest to the integration interval  $[-1, 1]$ , denoted by  $\{t_0, \bar{t}_0\}$ . Based on the assumptions below (3.4), we let  $C$  extend to infinity, leaving only the contributions along the deformations  $C_1$  and  $C_2$  illustrated in Figure 3.1,

$$(3.13) \quad E_{t, n_t} \Theta_p \approx \frac{1}{2\pi i} \int_{C_1} \frac{f(t, \varphi) k_{n_t}(t)}{(R^2(t, \varphi, \mathbf{x}))^p} \, dt + \frac{1}{2\pi i} \int_{C_2} \frac{f(t, \varphi) k_{n_t}(t)}{(R^2(t, \varphi, \mathbf{x}))^p} \, dt =: E_1 + E_2.$$

As the two error contributions are treated similarly, we consider only the contribution from  $C_1$ . To derive an estimate of  $E_1$ , we rewrite its integrand so that an explicit representation of the singularity  $t_0$  is obtained. Similar to the singularity swap quadrature (SSQ, [2]) method, this is done by swapping the singularity of the integrand to a simpler function,

$$(3.14) \quad E_1 = \frac{1}{2\pi i} \int_{C_1} f(t, \varphi) \left( \frac{t - t_0}{R^2(t, \varphi, \mathbf{x})} \right)^p \frac{k_{n_t}(t)}{(t - t_0)^p} \, dt.$$

Note that, just as in SSQ, if  $f(t, \varphi)$  is smooth, so is the factor  $f(t, \varphi)(t - t_0)^p / (R^2(t, \varphi, \mathbf{x}))^p$ . By assuming that it varies much slower than  $k_{n_t}$  and that the main contribution to the integral comes from the neighborhood around  $t_0$ , we make the approximation

$$(3.15) \quad E_1 \approx \frac{1}{2\pi i} f(t_0, \varphi) G_t(t_0, \varphi, \mathbf{x})^p \int_{C_1} \frac{k_{n_t}(t)}{(t - t_0)^p} \, dt.$$

Here, we introduce a so-called geometry factor  $G_t$ , which for a root  $w$  of  $R^2(t, \varphi, \mathbf{x})$  in  $t$  is defined as

$$(3.16) \quad G_t(w, \varphi, \mathbf{x}) = \lim_{t \rightarrow w} \frac{t - w}{R^2(t, \varphi, \mathbf{x})}.$$



The simplified integral (3.15) can then be well estimated by defining an appropriate branch cut. By repeating the same steps with the branch point  $\bar{t}_0$ , one can estimate the contribution along  $C_2$ . An estimate for the error associated with integrating (3.11) in the azimuthal  $\varphi$  direction can be derived similarly, with the error function  $k_{n,\varphi}(z)$  for the trapezoidal rule.

Once estimates for  $E_{t,n_t}\Theta_p$  and  $E_{\varphi,n_\varphi}\Theta_p$  in (3.12) have been derived, it remains to integrate these with respect to the remaining variable. Since this process is not related or essential for the subsequent derivations, we omit the details here. Instead, we refer to [42, Section 6], which provides a comprehensive explanation of how the integrals in (3.12) are simplified to be amenable to efficient numerical approximation. We point out that the final error estimate only requires the evaluation of one  $\varphi_0$  and one  $t_0$  root.

*Remark 3.1* (Evaluating quantities at the root). To evaluate the estimates needed for this work, functions such as  $f(t_0, \varphi)$  and  $G_t(t_0, \varphi, \mathbf{x})$  in (3.15), must be evaluated at the complex-valued root  $t_0$ . If these functions are analytically known, they can be computed directly. However, in practice, this is often not the case for  $f$  as it contains the layer density function, which is only known at the discretization points on the surface. In such cases, a local approximation  $\tilde{f}$  based on a Taylor expansion around the grid point closest to  $\mathbf{x}$  can be constructed, allowing  $\tilde{f}$  to be directly evaluated at  $t_0$  [3].

*Remark 3.2* (Extending an error estimate). In (3.15), we assumed that  $k_{n_t}$  was the most rapidly varying factor in the integrand (3.14), allowing smooth factors in the integrand to be moved outside the integral and evaluated at  $t_0$ . This technique, frequently used in this work, generalizes as follows. Suppose we have an error estimate,  $E^{\text{EST}}[g]$ , for a function  $g$  that has a singularity at  $t_0$ . Now, consider the function  $gm$ , where  $m$  is a smooth function that varies less than  $g$ . Then, the error estimate for  $gm$  can be approximated as

$$(3.17) \quad E^{\text{EST}}[gm] \approx |m(t_0)| E^{\text{EST}}[g].$$

In this way, we extend the estimate of  $g$  to account for  $m$ .

**3.3. Quadrature error estimates for adaptivity in polar direction.** Here, we focus on estimating the quadrature error of the function  $\Lambda^{\text{sq}}$ , defined in (2.25), repeated here for convenience,

$$(3.18) \quad \Lambda^{\text{sq}}(\theta, \mathbf{x}) = \left( \lambda(\theta) + \sqrt{\lambda(\theta)^2 - \rho^2 \sin^2(\theta)} \right)^{-1/2},$$

with  $\lambda$  defined in (2.2). This estimate is crucial for adaptively subdividing the interval in the case  $p = 1/2$ .

We begin by deriving an error estimate for a general  $n$ -point quadrature rule, followed by the specific case of the Gauss–Legendre rule. The final result is provided in *Error estimate 3.1*.

**3.3.1. General results.** Given an  $n$ -point quadrature rule with error function  $k_n(t)$  as introduced in (3.4), we aim to derive an estimate of the error in evaluating

$$(3.19) \quad \int_{\theta_a}^{\theta_b} \Lambda^{\text{sq}}(\theta, \mathbf{x}) \, d\theta = \int_E \Lambda^{\text{sq}}(\theta(t, \theta_a, \theta_b), \mathbf{x}) \theta_{\text{sc}} \, dt$$

denoted as  $E[\Lambda^{\text{sq}}](\mathbf{x}, n, \theta_a, \theta_b)$ , by following [23, 3]. Here,  $\theta(t, \theta_a, \theta_b)$  is the linear map between the base interval  $E$  and  $[\theta_a, \theta_b]$  in (1.5), and  $\theta_{\text{sc}}$  is the corresponding scaling factor. Let  $\{t_0^\lambda, \bar{t}_0^\lambda\}$  denote the branch points of the integrand closest to  $E$ , which are defined as roots of  $R_\lambda^2(\theta(t, \theta_a, \theta_b), \mathbf{x})$  in (2.22). For the remainder of Section 3, we will denote  $\theta(t, \theta_a, \theta_b)$  by  $\theta(t)$  and the roots  $\{t_0^\lambda, \bar{t}_0^\lambda\}$  by  $\{t_0, \bar{t}_0\}$ , for ease of notation.

Recalling results from Section 3.1, the quadrature error of (3.19) is given by a contour integral in the complex plane. By deforming the contour away from the integration interval  $E$ , the error is approximated by the contribution from the branch points  $\{t_0, \bar{t}_0\}$  and their branch cuts. Let  $C_1$  denote the curve going around  $t_0$  following the branch cut from  $t_0$  to  $\infty$ , and let  $C_2$  be defined analogously but instead with  $\bar{t}_0$ , as shown in Figure 3.1. Under the assumptions following (3.4), the quadrature error  $E[\Lambda^{\text{sq}}](\mathbf{x}, n, \theta_a, \theta_b)$  becomes

$$(3.20) \quad E[\Lambda^{\text{sq}}](\mathbf{x}, n, \theta_a, \theta_b) \approx \frac{1}{2\pi i} \int_{C_1} \Lambda^{\text{sq}}(\theta(t), \mathbf{x}) k_n(t) \theta_{\text{sc}} \, dt + \frac{1}{2\pi i} \int_{C_2} \Lambda^{\text{sq}}(\theta(t), \mathbf{x}) k_n(t) \theta_{\text{sc}} \, dt =: E_1 + E_2.$$

Consider the error contribution from  $C_1$ . The integrand has branch point singularities of the form  $(t - t_0)^{1/2}$  and  $(t - \bar{t}_0)^{1/2}$ , which we multiply and divide by to get (cf. (3.14))

$$(3.21) \quad E_1 = \frac{\theta_{\text{sc}}}{2\pi i} \int_{C_1} \frac{k_n(t)}{(\lambda(\theta(t)) + \bar{G}(\theta(t))^{1/2} \theta_{\text{sc}} (t - t_0)^{1/2} (t - \bar{t}_0)^{1/2})^{1/2}} dt,$$

where the function  $\bar{G}$  is defined by

$$(3.22) \quad \bar{G}(\theta) := \frac{\lambda(\theta)^2 - \rho^2 \sin^2(\theta)}{(\theta - \theta_0)(\theta - \bar{\theta}_0)}.$$

Let  $C_1^+$  denote the side of  $C_1$  going outwards, from  $t_0$  to  $\infty$ , and let  $C_1^-$  denote the other side going in the opposite direction such that  $C_1 = C_1^- \cup C_1^+$ , illustrated in Figure 3.1. Defining the jump across the branch cut as

$$(3.23) \quad (t - t_0) \Big|_{C_1^+} = (t - t_0) \Big|_{C_1^-} e^{-2\pi i},$$

we obtain

$$(3.24) \quad (t - t_0)^{1/2} \Big|_{C_1^+} = -(t - t_0)^{1/2} \Big|_{C_1^-}.$$

This allows us to express the contribution from  $C_1$  in two parts: an integral from  $t_0$  to  $\infty$  with  $(t - t_0)^{1/2} \Big|_{C_1^+}$ , and another from  $\infty$  to  $t_0$  with  $(t - t_0)^{1/2} \Big|_{C_1^-}$ . With the definition

$$(3.25) \quad J_{\pm}(t_0, n) := \int_{t_0}^{\infty} \frac{k_n(t)}{(\lambda(\theta(t)) \pm \bar{G}(\theta(t))^{1/2} \theta_{\text{sc}} (t - t_0)^{1/2} (t - \bar{t}_0)^{1/2})^{1/2}} dt,$$

we find  $E_1 = \frac{\theta_{\text{sc}}}{2\pi i} J(t_0, n)$ , where

$$(3.26) \quad J(t_0, n) = J_+(t_0, n) - J_-(t_0, n).$$

The error contribution  $E_2$  from  $C_2$  for the branch point  $\bar{t}_0$  is computed analogously and is found as  $E_2 = \bar{E}_1$ . By combining these terms, discarding the real part, and taking the absolute value, we estimate the error as

$$(3.27) \quad |E[\Lambda^{\text{sq}}](\mathbf{x}, n, \theta_a, \theta_b)| \approx \frac{\theta_{\text{sc}}}{\pi} |J(t_0, n)|.$$

For (3.27) to be useful, an efficient and sufficiently accurate way to evaluate the integrals in  $J$  is needed. We will now consider that problem in the case of the Gauss–Legendre rule.

**3.3.2. Gauss–Legendre rule.** For the Gauss–Legendre rule on  $E = [-1, 1]$ , the error function  $k_n$  does not have a closed form expression, but was shown in [21, 23] to satisfy the asymptotic formula

$$(3.28) \quad k_n(z) \simeq \frac{2\pi}{\xi(z)^{2n+1}}$$

as  $n \rightarrow \infty$  with  $\xi(z) = z + \sqrt{z^2 - 1}$ . Here, and for the remainder of this paper,  $\sqrt{z^2 - 1}$  is defined as  $\sqrt{z+1}\sqrt{z-1}$  with  $-\pi < \arg(z \pm 1) \leq \pi$ .

The integrand in (3.25) has a branch point at  $t_0$ . Following [23], we define a branch cut extending from  $t_0$  to  $\infty$  that avoids crossing the interval  $[-1, 1]$ ,

$$(3.29) \quad B(t_0) = \left\{ v(s) \in \mathbb{C} : v(s) = \frac{1}{2} \left( \zeta(s) + \frac{1}{\zeta(s)} \right), \quad 1 \leq s < \infty \right\},$$

where

$$(3.30) \quad \zeta(s) = \zeta_0 s, \quad \zeta_0 = t_0 + \sqrt{t_0^2 - 1}.$$

One may verify that, as intended,  $v(1) = t_0$ . This particular parametrization leads to the following helpful simplification of  $k_n$ ,

$$(3.31) \quad k_n(v(s)) \simeq \frac{2\pi}{\zeta(s)^{2n+1}},$$

where

$$(3.32) \quad \varrho(t_0) = |\zeta_0|$$

is the so-called Bernstein radius of  $t_0$ . With this, we write (3.25) as

$$(3.33) \quad J_{\pm}(t_0, n) \simeq \frac{2\pi}{\zeta_0^{2n+1}} \int_1^{\infty} \frac{1}{s^{2n+1}} \frac{v'(s) ds}{(\lambda(\theta(v(s)) \pm \bar{G}(\theta(v(s))))^{1/2} \theta_{sc}(v(s) - t_0)^{1/2} (v(s) - \bar{t}_0)^{1/2})^{1/2}},$$

which inserted into (3.27) yields (3.34) presented in *Error estimate 3.1*.

**ERROR ESTIMATE 3.1** (Gauss–Legendre quadrature,  $\Lambda^{sq}$ ). *Let  $\mathbf{x} = (x, y, z)$  be a target point with  $\rho = \sqrt{x^2 + y^2}$ , and let  $\gamma_{\rho}(\theta) = (a(\theta) \sin(\theta), b(\theta) \cos(\theta))$  parametrize a smooth curve in the  $\rho z$ -plane on the interval  $[\theta_a, \theta_b]$ . Denote by  $\{t_0, \bar{t}_0\}$  the closest pair of complex roots, with respect to  $E = [-1, 1]$ , of  $R_{\lambda}^2(\theta(t, \theta_a, \theta_b), \mathbf{x})$ , as defined in (2.22). The functions  $a(\theta)$  and  $b(\theta)$  are introduced in (1.4).*

*The quadrature error for evaluating the integral in (3.19) using an  $n$ -point Gauss–Legendre rule can, in the limit  $n \rightarrow \infty$ , be estimated as*

$$(3.34) \quad |E^Q[\Lambda^{sq}](\mathbf{x}, n, \theta_a, \theta_b)| \approx \alpha^Q(2n+1)\beta^Q(2n+1),$$

where

$$(3.35) \quad \alpha^Q(m) = \frac{2}{\varrho(t_0)^m} \theta_{sc}, \quad \beta^Q(m) = \left| U_+^Q(m) - U_-^Q(m) \right|,$$

and

$$(3.36) \quad U_{\pm}^Q(m) = \int_1^{\infty} \frac{1}{s^m} \frac{v'(s) ds}{(\lambda(\theta(v(s)) \pm \bar{G}(\theta(v(s))))^{1/2} \theta_{sc}(v(s) - t_0)^{1/2} (v(s) - \bar{t}_0)^{1/2})^{1/2}}.$$

Here, the functions  $\bar{G}$ ,  $v$ , and  $\varrho$  are defined in (3.22), (3.29), and (3.32), respectively.

**Remark 3.3** (Numerical evaluation of error estimate). The integrand of the branch cut integral in  $\beta^Q(2n+1)$  in (3.34) decays rapidly away from  $s = 1$  due to the factor  $s^{-(2n+1)}$  in (3.36), and is found to be surprisingly smooth for all target point locations. This decay permits truncation of the integration interval at  $1 < L^Q \ll \infty$ , enabling efficient approximation of the integral using Gauss–Legendre quadrature on  $[1, L^Q]$ . We find that 8 quadrature points usually yields sufficient accuracy. The truncation point  $L^Q$  is found such that  $s^{-(2n+1)}$  equals  $\kappa > 0$  at  $s = L^Q$ . We set  $\kappa = 10^{-10}$ .

**Remark 3.4** (Choice of branch cut parametrization). The particular parametrization of the branch cut in (3.29) has been crucial in deriving accurate analytical estimates of the error associated with the Gauss–Legendre rule in various contexts [23, 3, 42]. However, deriving such estimates for the integral in  $\beta^Q$  in (3.35) proved challenging as we require them to be sufficiently precise across all target point locations, notably for close evaluation. Instead, we opted for numerically integrating  $\beta^Q$ , as described in Remark 3.3, which proved to be both accurate and robust with regard to target point location, making the specific choice of branch cut parametrization less critical, with alternative parameterizations potentially working equally well. Nevertheless, the chosen parametrization simplifies the error function  $k_n$ , as shown in (3.31), which aids in determining an appropriate truncation point  $L^Q$  of the integration interval for the Gauss–Legendre quadrature rule, justifying its continued use.

**3.4. Interpolation error estimate for adaptivity in polar direction.** Here we derive an error estimate for polynomial interpolation of  $\Lambda^{\text{sq}}$  as defined in (3.18), following similar steps to those in Section 3.3. The interpolation is performed over the interval  $E = [-1, 1]$ , with the linear map  $\theta(t, \theta_a, \theta_b)$  defined in (1.5). Using the same notation as in Section 3.3, we find that

$$(3.37) \quad |E_n^I[\Lambda^{\text{sq}}](\mathbf{x}, \tau)| \approx \frac{1}{\pi} |\ell_n(\tau) (J_+^I(t_0, n) - J_-^I(t_0, n))|,$$

where the integral  $J^I$ , defined over the branch cut in (3.29)-(3.30), is given by

$$(3.38) \quad J_{\pm}^I(t_0, n) \approx \int_1^{\infty} \frac{1}{(v(s) - \tau)\ell_n(v(s))} \frac{v'(s) ds}{(\lambda(\theta(v(s)) + \bar{G}(\theta(v(s))))^{1/2} \theta_{\text{sc}}(v(s) - t_0)^{1/2} (v(s) - \bar{t}_0)^{1/2})^{1/2}}.$$

The main difference between (3.33) and (3.38) is the factor  $1/\ell_n(v(s))$ . Notably, as  $s \rightarrow \infty$ ,  $1/\ell_n(v(s))$  behaves as  $1/s^n$ , focusing the integrand's contribution near  $s = 1$ , where it can be approximated by  $1/\ell_n(t_0)$ . This leads to the following approximation

$$(3.39) \quad \ell_n(v(s)) \approx \ell_n(t_0) s^n, \quad 1 \leq s < \infty.$$

By substituting (3.39) into (3.38) and maximizing over  $\tau \in \{-1, 0, 1\}$ , we obtain the simplified form (3.40). This maximization is supported by numerical observations.

The final interpolation error estimate is given below, and is numerically evaluated using an analogous quadrature approximation as described in Remark 3.3. Compared to the quadrature error estimates in *Error estimate 3.1*, the  $n$ -dependence shifts from  $2n + 1$  to  $n$ , and the estimate now includes a maximum over different  $\tau$ -values.

**ERROR ESTIMATE 3.2** (Polynomial interpolation,  $\Lambda^{\text{sq}}$ ). *Consider the function  $\Lambda^{\text{sq}}$  defined by (3.18). Let everything be defined analogously to Error estimate 3.1. The error in the polynomial interpolant of degree at most  $n - 1$  for  $\Lambda^{\text{sq}}$ , as defined in (3.10), can be estimated as*

$$(3.40) \quad |E_n^I[\Lambda^{\text{sq}}](\mathbf{x}, n, \theta_a, \theta_b)| \approx \alpha^I(n) \max_{\tau \in \{-1, 0, 1\}} \beta^I(n, \tau),$$

where

$$(3.41) \quad \alpha^I(m) = \frac{1}{\pi |\ell_m(t_0)|}, \quad \beta^I(m, \tau) = |\ell_m(\tau) (U_+^I(m, \tau) - U_-^I(m, \tau))|,$$

with

$$(3.42) \quad U_{\pm}^I(m, \tau) = \int_1^{\infty} \frac{1}{s^m} \frac{1}{(v(s) - \tau)} \frac{v'(s) ds}{(\lambda(\theta(v(s)) \pm \bar{G}(\theta(v(s))))^{1/2} \theta_{\text{sc}}(v(s) - t_0)^{1/2} (v(s) - \bar{t}_0)^{1/2})^{1/2}},$$

where  $\ell_m$  is the  $m$ -point node polynomial defined in (3.7).

**3.5. Performance of error estimates for adaptivity.** We now demonstrate the performance of the derived quadrature and interpolation error estimates for  $\Lambda^{\text{sq}}$  in (3.18). Figure 3.2 shows that the estimates perform well for both the convex spheroid and the non-convex “smooth star” geometry across all target point positions, including those far from and close to the symmetry axis, for a fixed value of  $n$ .

Next, we study how effectively the estimates capture the error decay as  $n$  increases. We randomly distribute a large number of target points on one of the contours in Figure 3.2 for the spherical geometry, where the magnitude of the error is roughly constant. Since the Gauss–Legendre error function (3.28) remains constant along the level sets of the Bernstein radius function,  $\varrho$ , in (3.32), we begin by determining  $t_0^\lambda$  such that  $\varrho(t_0^\lambda) = P$ , where  $P$  is a constant. We then construct the corresponding target point  $\mathbf{x}(t_0^\lambda)$ , following the approach outlined in [3, Section 5.4]. The resulting target points are displayed in black in Figure 3.3a. Furthermore, we assess the performance of the estimates for close evaluation by placing target points on three lines normal to the surface, depicted in colors in Figure 3.3a.

Figure 3.3 presents the outcome of these experiments. In Figure 3.3b, the maximum absolute error across all target points is shown for different values of  $n$ . As  $n$  increases, the quadrature and interpolation errors both decrease, though at different rates, with their corresponding estimates closely following this behavior. The bottom row of plots, with  $n = 28$  fixed, demonstrate that the estimates provide good approximate upper bounds for target points both far away from and close to the surface.

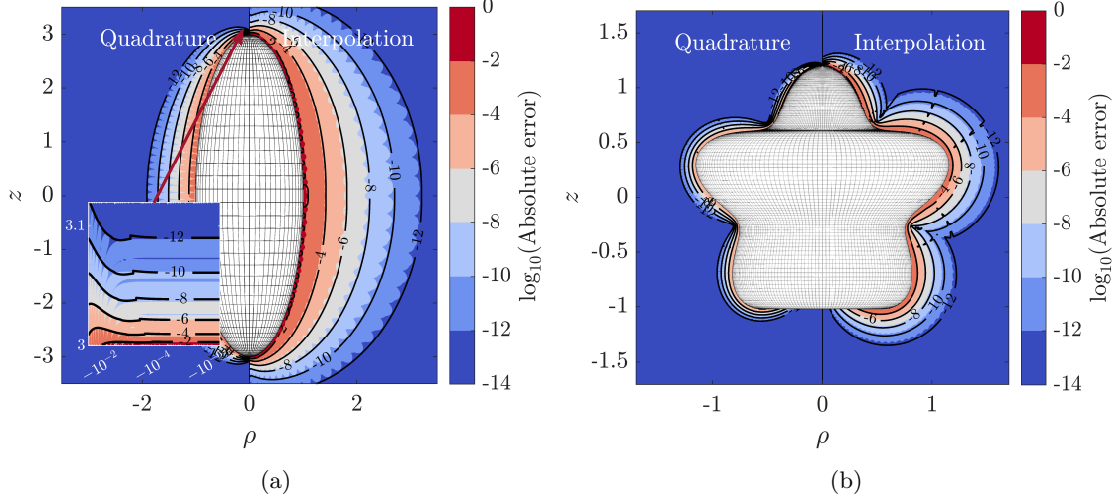


Fig. 3.2: Measured and estimated quadrature and interpolation error of  $\Lambda^{\text{sq}}$  in (3.18) on  $[0, \pi]$  in the  $\rho z$ -plane.

**4. Root finding.** The error estimates presented in the previous sections accurately predict the corresponding measured errors. However, evaluating these estimates for a given target point  $\mathbf{x}$  requires identifying the nearest complex-valued root of a squared-distance function. Specifically, the regular quadrature error estimate in Section 3.2 requires two roots of  $R^2(\theta, \varphi, \mathbf{x})$  in (1.7). In addition, the quadrature and interpolation error estimates in Sections 3.3-3.4 for the function  $\Lambda^{\text{sq}}$  in (3.18), rely on a root of  $R_\lambda^2(\theta, \mathbf{x})$  in (2.22). Thus, a total of three different roots are needed. We begin by presenting analytical results for finding these roots in spheroidal geometries, followed by a discussion of the general axisymmetric case.

**4.1. Analytical derivations for spheroidal geometries.** We begin with a result from [42] for finding the root of a squared-distance function defined with respect to a circle in the  $xy$ -plane. We then extend this result to an ellipse in the  $xy$ -plane and use it to derive an expression for the root of  $R_\lambda^2(\theta, \mathbf{x})$  in the case of a spheroid. Finally, we provide an analytical formula for the root of  $R^2(\theta, \varphi, \mathbf{x})$  in  $\theta$  (given  $\varphi$ ) for spheroidal geometries.

LEMMA 4.1 (Root of  $R^2$  for circle in plane [42]). *Let a circle of radius  $a > 0$  in the  $xy$ -plane be parameterized by  $(\gamma_1(\alpha), \gamma_2(\alpha), \gamma_3(\alpha)) = a(\cos(\alpha), \sin(\alpha), 0)$ ,  $0 \leq \alpha < 2\pi$ . Given a point  $\mathbf{x} = (x, y, z) \in \mathbb{R}^3$  with  $\rho = \sqrt{x^2 + y^2} > 0$ , not on the circle, define*

$$(4.1) \quad R^2(\alpha, \mathbf{x}) = (\gamma_1(\alpha) - x)^2 + (\gamma_2(\alpha) - y)^2 + z^2.$$

Then,  $R^2(\alpha, \mathbf{x}) = 0$  for  $\alpha = \alpha_0$ , with

$$(4.2) \quad \alpha_0 = \text{atan2}(y, x) \pm i \ln \left( \frac{1}{\rho} \left( \lambda + \sqrt{\lambda^2 - \rho^2} \right) \right), \quad \lambda = \frac{1}{2a} (a^2 + x^2 + y^2 + z^2).$$

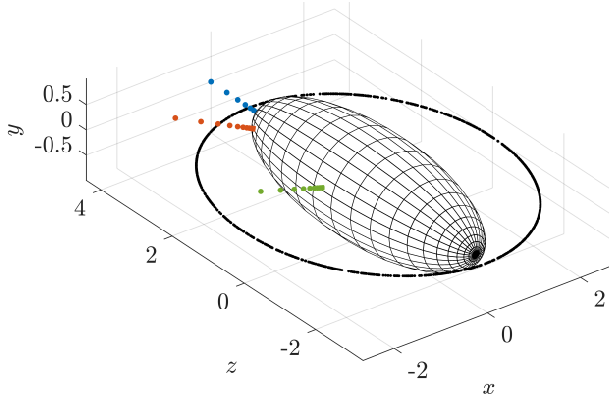
Here,  $\lambda > \rho$  and  $\text{atan2}(\eta, \xi)$  is the argument of the complex number  $\xi + i\eta$ ,  $-\pi < \text{atan2}(\eta, \xi) \leq \pi$ .

LEMMA 4.2 (Root of  $R^2$  for ellipse in plane). *Let an ellipse with semi-axes  $a, b > 0$  in the  $xy$ -plane be parameterized by  $(\gamma_1(\alpha), \gamma_2(\alpha)) = (a \cos(\alpha), b \sin(\alpha))$ ,  $0 \leq \alpha < 2\pi$ . Given a point  $\mathbf{x} = (x, y) \in \mathbb{R}^2$ , in the plane of the ellipse and not on it, define*

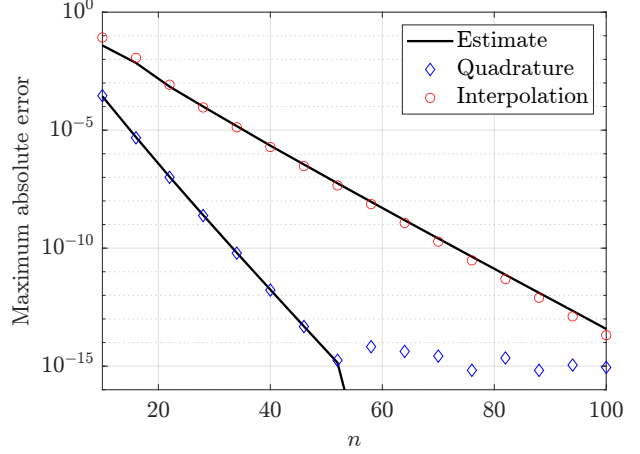
$$(4.3) \quad R^2(\alpha, \mathbf{x}) = (a \cos(\alpha) - x)^2 + (b \sin(\alpha) - y)^2.$$

Then,  $R^2(\alpha, \mathbf{x}) = 0$  for  $\alpha = \alpha_0$ , with

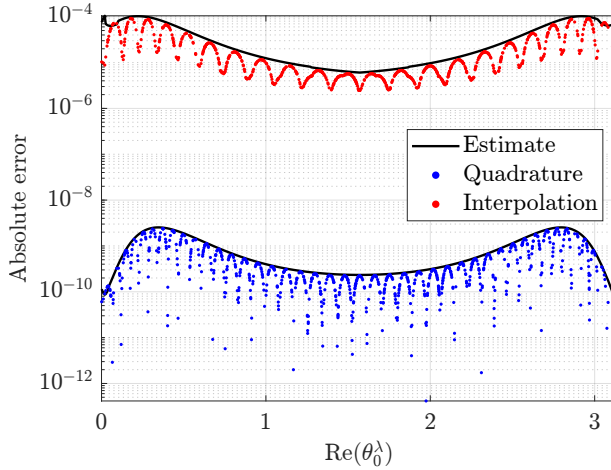
$$(4.4) \quad \alpha_0 = \text{atan2}(\tilde{y}, \tilde{x}) \pm i \ln \left( \frac{1}{\rho} \left( \lambda + \sqrt{\lambda^2 - \rho^2} \right) \right), \quad \lambda = \frac{1}{2a} (\tilde{a}^2 + \tilde{x}^2 + \tilde{y}^2),$$



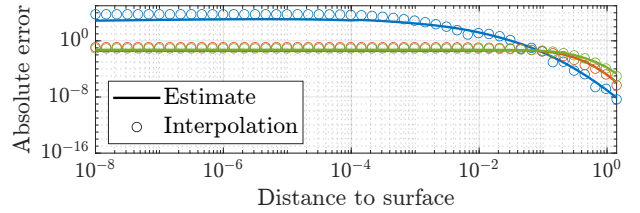
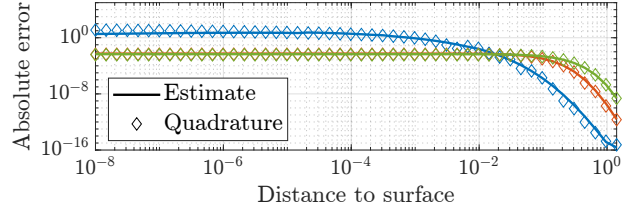
(a) Source geometry, 1000 black target points with  $\varrho(t_0^\lambda) = 3$  and colored target points along lines normal to the surface with fixed  $\varphi = 10\pi/11$  and  $\theta = \{0, 0.6, \pi/2\}$ .



(b) Maximum absolute errors and estimates over all black target points in (a).



(c) Pointwise errors and estimates with  $n = 28$  from (b).



(d) Pointwise errors and estimates using  $n = 28$  for the colored target points in (a).

Fig. 3.3: Measured and estimated quadrature and interpolation error for the function  $\Lambda^{\text{sq}}$  in (3.18) on  $[0, \pi]$ .

where  $\tilde{a} = (a + b)/2$ ,  $\tilde{x} = \text{Re}(u)$ ,  $\tilde{y} = \text{Im}(u)$ , and

$$(4.5) \quad u = \frac{1}{2} \left( w \pm \sqrt{w^2 - 4c^2} \right).$$

Here,  $w = x + iy$ ,  $c^2 = (a^2 - b^2)/4$  and  $\text{atan2}$  is defined as in Lemma 4.1.

*Proof.* Consider the Joukowski transform

$$(4.6) \quad w = w(u) = u + \frac{c^2}{u},$$

where  $u \in \mathbb{C} \setminus \{0\}$  for some constant  $c$ . The Joukowski transform is a conformal mapping if  $u \neq 0$  and  $u \neq \pm 1$ , that maps a circle from the  $u$ -plane into a transformed shape (in this case an ellipse), in the  $w$ -plane.



Conversely, its inverse,

$$(4.7) \quad u = \frac{1}{2} \left( w \pm \sqrt{w^2 - 4c^2} \right),$$

maps in the other direction.

Consider the circle  $\tilde{a}(\cos(\alpha), \sin(\alpha), 0)$  with radius  $\tilde{a} > 0$  in the  $xy$ -plane. Using (4.6) it is mapped into the ellipse  $(a \cos(\alpha), b \sin(\alpha), 0)$  in the same plane with semi-axes

$$(4.8) \quad a = \tilde{a} + \frac{c^2}{\tilde{a}} \quad \text{and} \quad b = \tilde{a} - \frac{c^2}{\tilde{a}}.$$

From (4.8), we have  $\tilde{a} = (a + b)/2$ , and  $c^2 = (a^2 - b^2)/4$ . Using the inverse map (4.7), a point in the coordinates of the ellipse is mapped back to the coordinates of the circle. Thus, for  $w = x + iy$ , we obtain  $u = \tilde{x} + i\tilde{y}$ . The situation is then as in Lemma 4.1, but now involving the circle  $\tilde{a}(\cos(\alpha), \sin(\alpha), 0)$  and a point  $(\tilde{x}, \tilde{y}, 0)$ .  $\square$

LEMMA 4.3 (Root of  $R_\lambda^2$ ). *Let  $\gamma(\theta, \varphi)$  be a spheroid parameterized as in (1.4) with semi-axes  $a(\theta) = a > 0$  and  $b(\theta) = b > 0$ . Given a target point  $\mathbf{x} = (x, y, z) \in \mathbb{R}^3$  with  $\rho = \sqrt{x^2 + y^2} > 0$  not on  $\gamma(\theta, \varphi)$ , define*

$$(4.9) \quad R_\lambda^2(\theta, \mathbf{x}) = (a \sin(\theta) - \rho)^2 + (b \cos(\theta) - z)^2.$$

Then,  $R_\lambda^2(\theta, \mathbf{x}) = 0$  for  $\theta = \theta_0^\lambda$ , where

$$(4.10) \quad \theta_0^\lambda = \text{atan2}(\tilde{y}, \tilde{x}) \pm i \ln \left( \frac{1}{\rho} \left( \lambda + \sqrt{\lambda^2 - \rho^2} \right) \right), \quad \lambda = \frac{1}{2a} (\tilde{a}^2 + \tilde{x}^2 + \tilde{y}^2),$$

with  $\tilde{a} = (a + b)/2$ ,  $\tilde{x} = \text{Re}(u)$ ,  $\tilde{y} = \text{Im}(u)$ , and

$$(4.11) \quad u = \frac{1}{2} \left( w \pm \sqrt{w^2 - 4c^2} \right).$$

Here,  $w = z + i\rho$ ,  $c^2 = (b^2 - a^2)/4$  and  $\text{atan2}$  is defined as in Lemma 4.1.

*Proof.* This follows directly from Lemma 4.2 by exchanging the roles of  $a$  and  $b$ , and letting the point be  $(z, \rho)$ .  $\square$

We now derive an analytical formula for the root of the squared distance function  $R^2(\theta, \varphi, \mathbf{x})$  in  $\theta$ , given  $\varphi$ . This derivation was carried out in [42] for a spherical geometry, and here, we extend these results to spheroidal shapes. Note that a formula for the root in the  $\varphi$  direction for a general axisymmetric geometry was previously given in Lemma 2.1.

LEMMA 4.4 (Root of  $R^2$  in  $\theta$  given  $\varphi$ ). *Let the spheroid  $\gamma(\theta, \varphi)$  be parameterized as in (1.4) with  $a(\theta) = a > 0$ ,  $b(\theta) = b > 0$ ,  $a \neq b$ . Given a target point  $\mathbf{x} = (x, y, z) \in \mathbb{R}^3$  not on  $\gamma$ , define*

$$(4.12) \quad R^2(\theta, \varphi, \mathbf{x}) = (\gamma_1(\theta, \varphi) - x)^2 + (\gamma_2(\theta, \varphi) - y)^2 + (\gamma_3(\theta, \varphi) - z)^2.$$

Given  $\varphi = \bar{\varphi} \in [0, 2\pi)$ , assume that if  $z = 0$ , then  $\bar{\varphi} - \text{atan2}(y, x) \neq \pi/2 + p\pi$ ,  $p \in \mathbb{Z}$ . Then,  $R^2(\theta, \bar{\varphi}, \mathbf{x}) = 0$  for  $\theta = \theta_0$ , with

$$(4.13) \quad \theta_0 = \text{Arg}(\beta) - i \ln(|\beta|),$$

where  $\beta$  satisfies the quartic equation,

$$(4.14) \quad \frac{\Delta}{4} \beta^4 + \tau \beta^3 + \left( \frac{\Delta}{2} + d^2 \right) \beta^2 + \bar{\tau} \beta + \frac{\tau}{4} = 0.$$

Here,

$$(4.15) \quad \Delta = b^2 - a^2, \quad \tau = -bz + ia(x \cos(\bar{\varphi}) + y \sin(\bar{\varphi})), \quad d = a^2 + x^2 + y^2 + z^2,$$

and  $\bar{\tau}$  denotes the complex conjugate of  $\tau$ .

*Proof.* With  $\varphi = \bar{\varphi}$ , the squared distance function  $R^2(\theta, \varphi, \mathbf{x})$  in (4.12) can be written as

$$(4.16) \quad R^2(\theta, \bar{\varphi}, \mathbf{x}) = a^2 \sin^2(\theta) + b^2 \cos^2(\theta) + x^2 + y^2 + z^2 - 2a(x \cos(\bar{\varphi}) + y \sin(\bar{\varphi})) \sin(\theta) - 2bz \cos(\theta).$$

Next, we make the ansatz  $\theta_0 = -i\eta$ ,  $\eta = \ln(\beta)$  for some  $\beta \in \mathbb{C}$  with  $0 = R^2(\theta_0, \bar{\varphi}, \mathbf{x})$ . Inserting the ansatz into (4.16) gives

$$(4.17) \quad 0 = \frac{1}{2} \left( a^2 + b^2 + 2(x^2 + y^2 + z^2) - 4bz \cosh(\eta) + (b^2 - a^2) \cosh(2\eta) + 4ia(x \cos(\bar{\varphi}) + y \sin(\bar{\varphi})) \sinh(\eta) \right).$$

We then express the trigonometric functions in exponential form, substituting  $\eta = \ln(\beta)$ . This leads to the quartic equation (4.14)-(4.15), which can be solved analytically for  $\beta$  if  $a \neq b$ . This quartic equation has four possible solutions, giving us four roots. In practice, we pick the root with the smallest imaginary part in terms of its magnitude. Using the complex logarithm, the ansatz  $\theta_0 = -i \ln(\beta)$  yield (4.13).  $\square$

**4.2. General axisymmetric geometries.** The analytical results in Lemma 4.3-4.4 apply specifically to spheroids. For a general axisymmetric geometry, only the root  $\varphi_0$  of  $R^2(\theta, \varphi, \mathbf{x})$ , defined by (1.7), can be obtained analytically. Fortunately, the other two roots needed in this work can be efficiently found using a one-dimensional Newton iteration.

For instance, to find a root  $\theta_0$  of  $R^2(\theta, \varphi, \mathbf{x})$  for a given target point  $\mathbf{x}$  and azimuthal angle  $\varphi$ , we follow the approach outlined in [42]. We first identify the polar angle  $\theta^*$  corresponding to the closest discrete point on the surface  $\gamma$  to  $\mathbf{x}$ . Using  $\theta^* + i/10$  as an initial guess for  $\theta_0$ , the Newton iteration typically converges to a strict tolerance within 10 iterations. In the rare cases where convergence is not achieved, we rerun the iteration using over-relaxation.

**5. A note on computational complexity.** The analysis below is based on a surface discretization with an  $n_\varphi$ -point trapezoidal rule and an  $n_t$ -point Gauss–Legendre panel in the azimuthal and polar direction, respectively, where we assume that values of the layer density are known at these discrete points. If several Gauss–Legendre panels are used in the polar direction, this discussion applies to each panel.

Through adaptive refinement in the polar direction, the final evaluation involves  $n_\varphi \times n_{\text{pan}} n_{\text{GL}}$  points. A significant contribution to the computational cost of the algorithm comes from interpolating the layer density onto this refined grid. For each of the  $n_\varphi$  discrete  $\varphi$  values, this is a one-dimensional interpolation in  $t$ , from  $n_t$  points to  $n_{\text{pan}} n_{\text{GL}}$  points, yielding a total cost of  $\mathcal{O}(n_\varphi n_{\text{pan}} n_{\text{GL}} n_t)$ .

Let  $n_{\text{pan}}^{\text{SSQ}, \varphi}$  represent the number of panels where the singularity swap quadrature (SSQ) method is invoked in the  $\varphi$  direction, leaving  $n_{\text{pan}}^{\text{TZ}}$  panels where the trapezoidal rule is applied, such that  $n_{\text{pan}} = n_{\text{pan}}^{\text{SSQ}, \varphi} + n_{\text{pan}}^{\text{TZ}}$ . A one-dimensional FFT with  $n_\varphi$  points must be computed in the  $\varphi$  direction for  $n_{\text{pan}}^{\text{SSQ}, \varphi} n_{\text{GL}}$  number of  $t$ -values, leading to a total cost of  $\mathcal{O}(n_{\text{pan}}^{\text{SSQ}, \varphi} n_{\text{GL}} n_\varphi \log(n_\varphi))$ . Applying the SSQ algorithm then invokes a cost of  $\mathcal{O}(n_\varphi n_{\text{pan}}^{\text{SSQ}, \varphi} n_{\text{GL}})$ , and similarly for the trapezoidal rule  $\mathcal{O}(n_\varphi n_{\text{pan}}^{\text{TZ}} n_{\text{GL}})$ . The remaining steps in the polar direction entails evaluation of one-dimensional integrals, resulting in computational cost that is subdominant to these first steps. The number of  $n_{\text{GL}}$ -point Gauss–Legendre panels,  $n_{\text{pan}}$ , determined by the adaptive algorithm for a given value of  $n_{\text{GL}}$ , primarily depends on the location of the target point  $\mathbf{x}$  and the error tolerance  $\epsilon$ . Consequently, we can write the dominant terms for the total computational cost as

$$(5.1) \quad C_1(\epsilon, \mathbf{x}, n_{\text{GL}}) n_t n_\varphi + C_2(\epsilon, \mathbf{x}, n_{\text{GL}}) n_\varphi \log(n_\varphi),$$

where  $C_1, C_2 > 0$ .

The discussion above assumes that  $k(\mathbf{x}, \mathbf{y})$  in (1.1) depends on  $\mathbf{x}$ . However, if  $k(\mathbf{x}, \mathbf{y})$  is independent of  $\mathbf{x}$ , the Fourier coefficients of  $f$  can be computed once in a precomputation step. Interpolation can then be performed on these Fourier coefficients for each of the  $n_{\text{pan}}^{\text{SSQ}, \varphi}$  panels adaptively set for the specific target point, thereby eliminating the second term in (5.1).

**6. Numerical experiments.** This section serves to numerically demonstrate the adaptivity and error control of the proposed *singularity swap surface quadrature (S3Q)* method. We evaluate various layer potentials defined over different axisymmetric geometries, aiming to achieve a specified error tolerance  $\epsilon$ . The

measured error is obtained by comparing our approximate layer potential values to reference values either known analytically or computed using an adaptive quadrature routine (the `integral2` function in MATLAB R2022b with `AbsTol=1e-14` and `RelTol=1e-14`).

In the following numerical experiments, we assume that both the parametrization of the geometry and the layer density function are analytically known. The values of  $n_t$  and  $n_\varphi$  are chosen to ensure the geometry and surfaces values are well resolved.

**6.1. Spheroids.** Spheroids are special as the complex-valued roots of the two squared distance functions are found analytically. To assess the S3Q method, we evaluate the harmonic layer potentials on two types of spheroids. A spheroid with aspect ratio 1: $X$ , i.e.  $a(\theta) = 1$  and  $b(\theta) = X$ , is referred to as a type  $SX$  spheroid. Target points are sampled on a uniform  $200 \times 200$  grid in the  $xz$ -plane at a fixed  $y = 0$ , as illustrated in Figure 1.1a.

**6.1.1. Harmonic single layer: Type S3.** We compute the harmonic single layer potential ( $p = 1/2$ )

$$(6.1) \quad u(\mathbf{x}) = \int_S \frac{\sigma(\mathbf{y})}{\|\mathbf{y} - \mathbf{x}\|} dS(\mathbf{y})$$

on a type S3 spheroid for the error tolerances  $\epsilon = 10^{-4}$ ,  $10^{-6}$ ,  $10^{-8}$ . The layer density function is given by

$$(6.2) \quad \sigma(\gamma(\theta, \varphi)) = \sin(5\theta)e^{-\cos^2(\varphi)} + 1.03.$$

Figure 6.1 presents the results with  $n_t = n_\varphi = 40$  and  $n_{GL} = 32$ . The top row plots show that the regular quadrature error estimate accurately identifies the target points where S3Q must be used, for which the measured errors are close to the desired tolerance  $\epsilon$ . As  $\epsilon$  decreases, the number of Gauss–Legendre panels,  $n_{\text{pan}}$ , set by the adaptive algorithm in the polar direction generally increases, as shown in Figure 6.1c. Despite the close proximity of target points to the surface, the maximum  $n_{\text{pan}}$  required to achieve the desired error tolerances  $\epsilon = 10^{-4}$ ,  $10^{-6}$ ,  $10^{-8}$  was 5, 10 and 14, respectively. For  $\epsilon = 10^{-8}$ , this maximum was reached at only one target point situated approximately  $5.2 \cdot 10^{-5}$  from the surface.

**6.1.2. Harmonic double layer: Type S10.** Next, we demonstrate the capabilities of S3Q for a spheroid with a high aspect ratio and examine how  $n_{\text{pan}}$  varies with distance between the target points and the surface. Specifically, we evaluate the harmonic double layer potential ( $p = 3/2$ )

$$(6.3) \quad u(\mathbf{x}) = \int_S \frac{\mathbf{n}_y \cdot (\mathbf{y} - \mathbf{x}) \sigma(\mathbf{y})}{\|\mathbf{y} - \mathbf{x}\|^3} dS(\mathbf{y})$$

on a type S10 spheroid with  $\epsilon = 10^{-8}$ , using the layer density function

$$(6.4) \quad \sigma(\gamma(\theta, \varphi)) = 1 + \sin(6\varphi + \theta) \sin(\theta)^2.$$

Here,  $\mathbf{n}_y$  denotes the outwards-pointing normal vector at  $\mathbf{y} \in S$ .

Figure 6.2 shows that the measured error generally is kept below  $\epsilon$ , with only 48 out of 30354 target points slightly exceeding this tolerance. The figure also highlights how  $n_{\text{pan}}$  varies with the relative location of the target point  $\mathbf{x}$  to the surface. Figure 6.3 further reveals a log-linear increase in  $n_{\text{pan}}$  as  $\mathbf{x}$  approaches the surface, independent of  $\epsilon$ . Note that the surface mesh depicted in Figure 6.2 represents the base discretization with  $n_t = 160$  and  $n_\varphi = 100$ , but that each adaptively set Gauss–Legendre panel in the polar direction only contains  $n_{GL} = 16$  points, such that  $n_{\text{pan}} = 10$  yields the same number of quadrature points as the base discretization.

**6.2. Stokes double layer: Axisymmetric geometry.** We now evaluate the Stokes double layer potential  $\mathbf{u}$  ( $p = 5/2$ ) using S3Q on the axisymmetric “peanut” geometry shown in Figure 1.1b. The three components are given by<sup>5</sup> ( $i = 1, 2, 3$ ),

$$(6.5) \quad u_i(\mathbf{x}) = \int_S T_{ijk}(\mathbf{x} - \mathbf{y}) \sigma_j(\mathbf{y}) n_k(\mathbf{y}) dS, \quad T_{ijk}(\mathbf{r}) = -6 \frac{r_i r_j r_k}{\|\mathbf{r}\|^5},$$

<sup>5</sup>The Einstein summation convention is applied here, where summation over repeated indices in a term is implied.

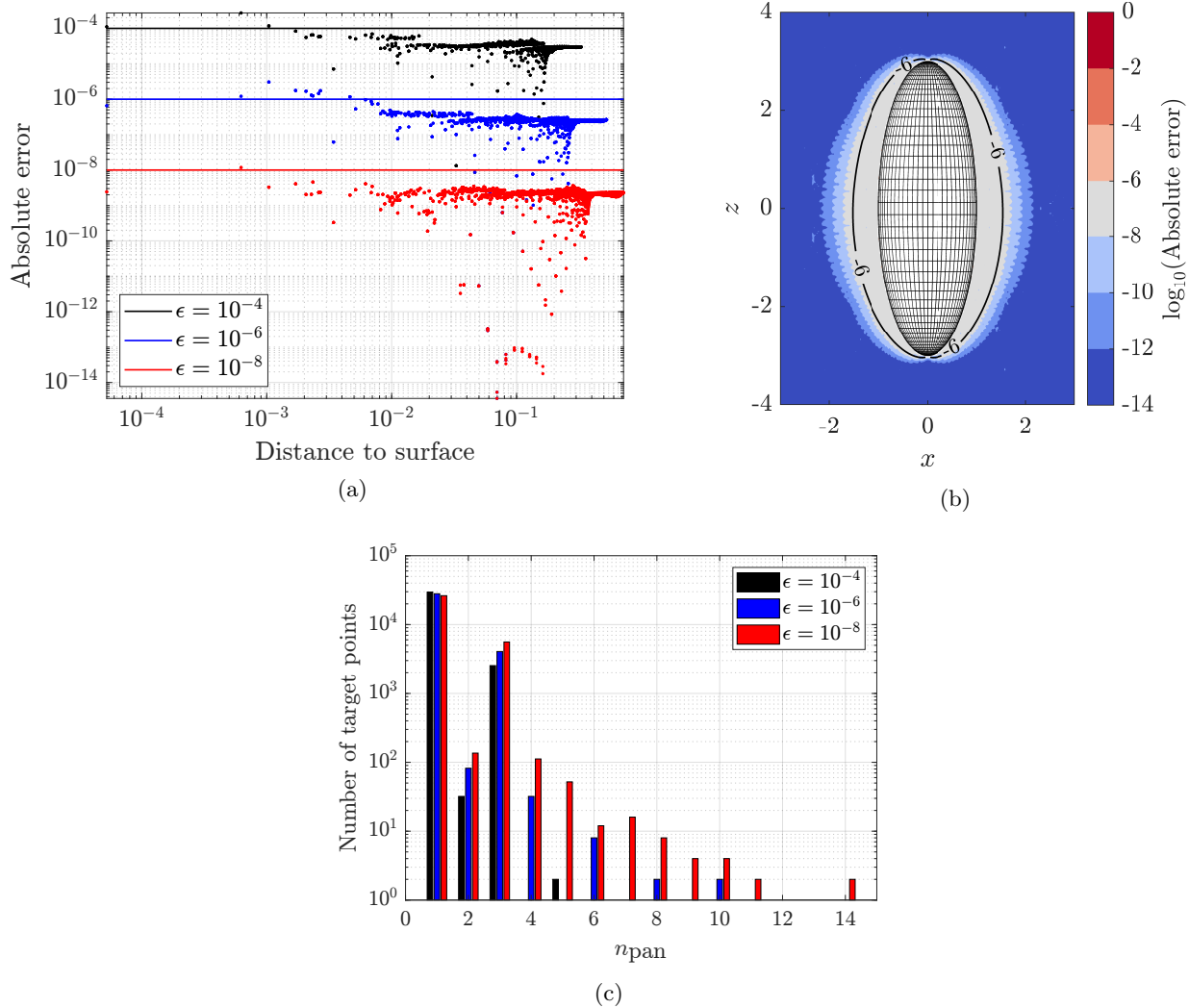


Fig. 6.1: Harmonic single layer potential computed using the singularity swap surface quadrature (S3Q) with different error tolerances  $\epsilon$ . Panel (a) shows how the measured error for each target point where S3Q was used stay close to  $\epsilon$ . Panel (b) illustrates the measured error and the contour level where the regular quadrature error estimate equals  $\epsilon = 10^{-6}$ . Panel (c) shows how the distribution of  $n_{\text{GL}}$ -point Gauss–Legendre panels,  $n_{\text{pan}}$ , set by the adaptive algorithm in the polar direction varies with  $\epsilon$ .

where the tensor  $T_{ijk}$  is known as the stresslet. For any constant layer density vector  $\tilde{\sigma}$ , the layer potential satisfies the so-called stresslet identity [39]

$$(6.6) \quad \mathbf{u}(\mathbf{x}) = \begin{cases} \mathbf{0}, & \text{if } \mathbf{x} \text{ is outside } S, \\ 4\pi\tilde{\sigma}, & \text{if } \mathbf{x} \in S, \\ 8\pi\tilde{\sigma}, & \text{if } \mathbf{x} \text{ is inside } S. \end{cases}$$

Figure 6.4 demonstrates the stresslet identity error, measured in the pointwise max norm, for two error tolerances  $\epsilon$  where  $n_t = 320$ ,  $n_\varphi = 180$  and  $n_{\text{GL}} = 16$ . Target points are sampled on a uniform  $200 \times 200$  grid in the  $xz$ -plane at a fixed  $y = 0$ . The results are summarized in Table 6.1. The results again show that S3Q is only activated when regular quadrature is deemed insufficient and that it in these cases successfully

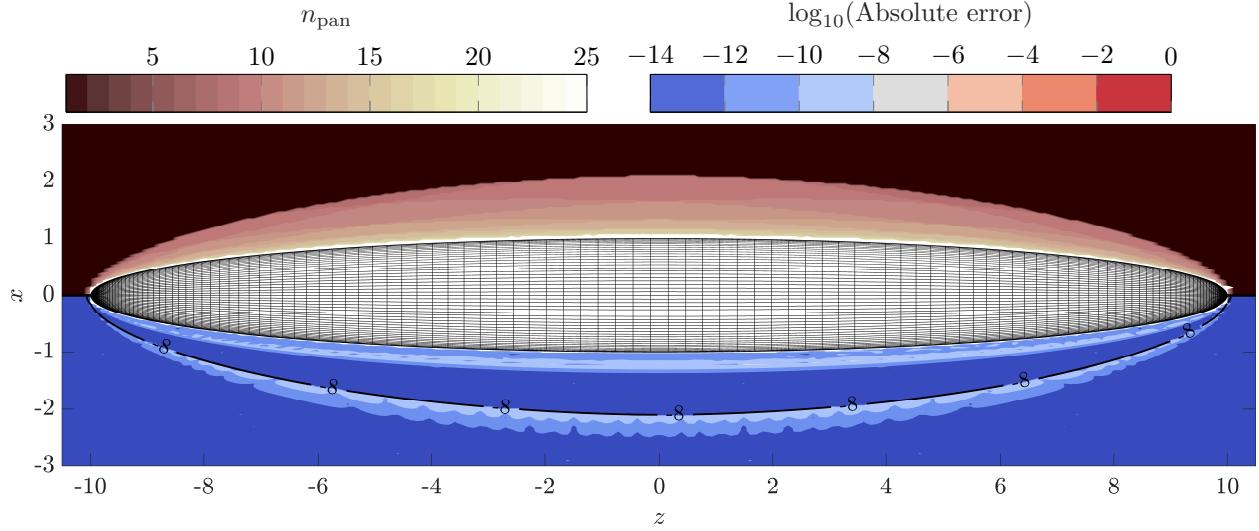


Fig. 6.2: Harmonic double layer potential computed using the singularity swap surface quadrature (S3Q) with error tolerance  $\epsilon = 10^{-8}$ . The upper and lower parts show the number of  $n_{\text{GL}}$ -point Gauss–Legendre panels,  $n_{\text{pan}}$ , set by the adaptive algorithm in the polar direction and the measured error, respectively. The maximum error is  $2.6 \cdot 10^{-8}$ , with the nearest target point approximately  $2.6 \cdot 10^{-3}$  from the surface. Here,  $n_t = 160$ ,  $n_\varphi = 100$  and  $n_{\text{GL}} = 16$ .

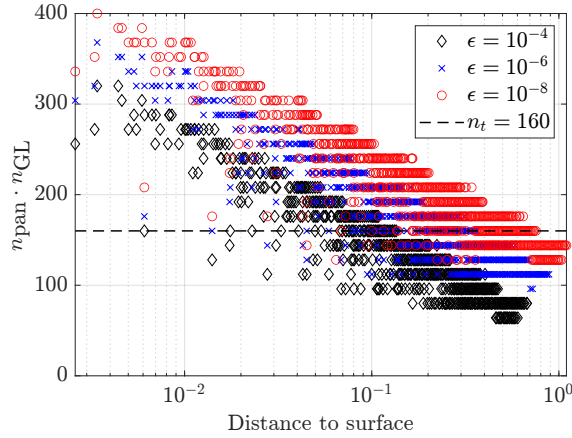


Fig. 6.3: Number of discretization points in the polar direction,  $n_{\text{pan}}n_{\text{GL}}$ , required to meet a specified error tolerance  $\epsilon$ . The dashed line represents the number of points in the base discretization in the polar direction. The problem setup is as in Figure 6.2.

keeps the errors close to the specified tolerances. Although a few points exceed these tolerances, the errors remain controlled and limited.

*Remark 6.1* (Very close evaluations). For target points very close to the surface, numerical results indicate that the error in evaluating the layer potential using the S3Q method can increase significantly, primarily due to catastrophic cancellation. This is particularly evident for strongly singular layer potentials, such as the Stokes double layer potential with  $p = 5/2$ . Target points where the error introduced by cancellation exceeds the desired error tolerance are referred to as invalid target points, as indicated in Table 6.1. We observe that this error scales as  $\mathcal{O}(1/d^{2(p-1)})$ , where  $d$  denotes the shortest distance between the target point

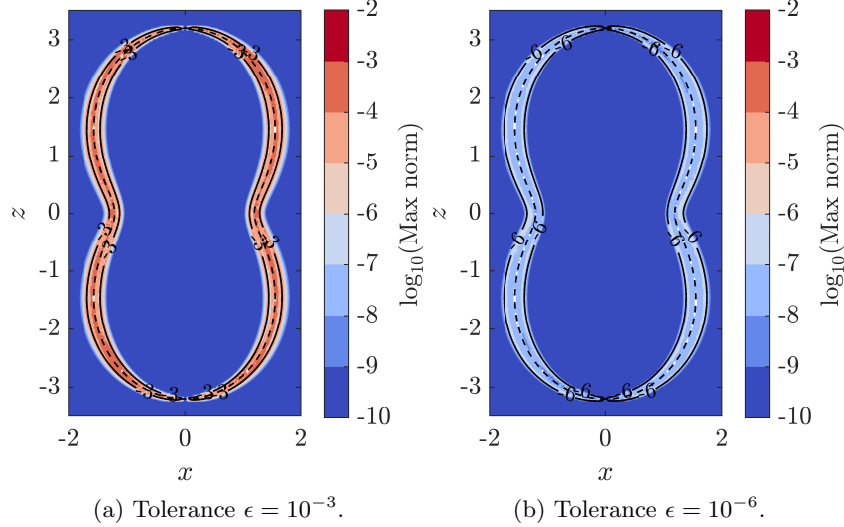


Fig. 6.4: Stresslet identity error using S3Q with two error tolerances  $\epsilon$ . The results are shown for target points both inside and outside of the “peanut”, which is indicated by the dashed black line. The solid black lines indicate the quadrature error estimate at the level  $\epsilon$ .

Table 6.1: Stresslet identity test inside and outside the “peanut” geometry shown in Figure 1.1b, using S3Q with two error tolerances  $\epsilon$ . The maximum error remains close to  $\epsilon$ , with only a few target points exceeding it. The setup is identical to that of Figure 6.4. Errors and minimum distances are calculated for valid target points only, as described in Remark 6.1. The symbol # denotes the number of target points.

Tolerance $\epsilon$	Max error ( $\# > \epsilon$ )	Min distance to surface	# valid (# S3Q)	# invalid
$10^{-3}$	$2.2 \cdot 10^{-3}$ (58)	$4.4 \cdot 10^{-4}$	39980 (3988)	20
$10^{-6}$	$1.5 \cdot 10^{-6}$ (3)	$5.9 \cdot 10^{-4}$	39880 (6292)	120

and the surface, with the error typically larger for target points near the geometry’s equator.

The S3Q method thus addresses most of the region between the surface and the area where regular quadrature suffices, leaving only a thin layer closest to the surface where it should not be directly applied.

**7. Conclusions.** The work presents an adaptive quadrature scheme for evaluating nearly singular layer potentials over axisymmetric surfaces, based on a given surface discretization. This special quadrature method requires only the desired error tolerance, and optionally the order of the Gauss–Legendre quadrature used in the adaptive polar direction, as user-defined parameters. Guided by an error estimate from [42], the method automatically switches from regular quadrature to the *singularity swap surface quadrature (S3Q)* method when needed, where all algorithmic choices and parameter values are automatically set to meet the specified error tolerance.

In the S3Q method, we combine a singularity swap quadrature method (SSQ, [2, 1, 10]) with a local adaptive discretization procedure. To enable the evaluation of surface integrals, we extended the SSQ method to handle additional kernels in 3D. The S3Q method first integrates the layer potential in the azimuthal direction using either the SSQ method or the trapezoidal rule, based on a quadrature error estimate for the latter. Analysis of the resulting integral in the polar direction reveals two critical functions: one with a nearly singular derivative and another with nearly singular behavior of one degree lower compared to the original layer potential. We employ the SSQ method only when the nearly singular behavior demands it, and use regular Gauss-Legendre quadrature otherwise. Both integration techniques rely on an adaptive subdivision of the interval in the polar direction into segments/panels, governed by error estimates for quadrature and



interpolation of the function with the nearly singular derivative. The number of panels in the polar direction will depend on the proximity of target points to the surface and the desired accuracy.

These new error estimates were derived through complex analysis. Using the Hermite interpolation formula, we extended the analytical framework of [3], originally developed for quadrature error estimation, to obtain remarkably accurate interpolation error estimates. The singularity swapping procedure, used in both the SSQ method and the error estimate derivations, relies on analytically continuing squared-distance functions and identifying their complex-valued roots. For spheroidal geometries, we provide new analytical expressions for these roots, while for general axisymmetric surfaces, a one-dimensional Newton iteration has proven to be sufficiently effective.

We demonstrate the error control capabilities of the S3Q method on harmonic and Stokes flow layer potentials over various axisymmetric geometries and different error tolerances. The results show that the measured error generally remains below the specified tolerance, and for the small fraction of target points where it does not, the error is not much larger than the tolerance. However, when target points are very close to the surface, the method faces limitations due to numerical cancellation, particularly evident in evaluating the Stokes double layer potential due to its  $1/r^5$  singularity. For robust and high-precision evaluations in this thin region, the S3Q method is best used in combination with some other methodology, such as asymptotic approximations [17] or by extrapolation or interpolation techniques (the hedgehog method [48, 8]). For the latter, the S3Q method can be used to evaluate the layer potential at points just outside this thin layer, allowing for accurate results as extrapolation distances are short.

Our current implementation of the S3Q method emphasizes its capabilities, and leaves room for efficiency improvements. For example, precomputation could accelerate the one-dimensional interpolations of the layer density (requiring a modification to the adaptive grid) and the evaluation of the SSQ coefficients in the azimuthal direction. Although this work has focused on single and double layer potentials for the Laplace and Stokes equations, it can be extended to the Helmholtz equation through kernel splitting [28]. Future work includes this extension, a robust treatment of target points very close to the surface where the evaluation is prone to numerical cancellation errors, and an efficient implementation of the S3Q method.

**8. Acknowledgments.** The authors would like to thank Ludvig af Klinteberg at the Department of Mathematics and Physics, Mälardalen University, for helpful discussions. The authors acknowledge the support from the Swedish Research Council under grant no. 2019-05206.

#### REFERENCES

- [1] L. AF KLINTEBERG, *Singularity swap quadrature for nearly singular line integrals on closed curves in two dimensions*, BIT Numerical Mathematics, 64 (2024), p. 11.
- [2] L. AF KLINTEBERG AND A. H. BARNETT, *Accurate quadrature of nearly singular line integrals in two and three dimensions by singularity swapping*, BIT Numerical Mathematics, 61 (2021), pp. 83–118.
- [3] L. AF KLINTEBERG, C. SORGENTONE, AND A.-K. TORBERG, *Quadrature error estimates for layer potentials evaluated near curved surfaces in three dimensions*, Computers & Mathematics with Applications, 111 (2022), pp. 1–19.
- [4] L. AF KLINTEBERG AND A.-K. TORBERG, *A fast integral equation method for solid particles in viscous flow using quadrature by expansion*, Journal of Computational Physics, 326 (2016), pp. 420–445.
- [5] L. AF KLINTEBERG AND A.-K. TORBERG, *Error estimation for quadrature by expansion in layer potential evaluation*, Advances in Computational Mathematics, 43 (2017), pp. 195–234.
- [6] L. AF KLINTEBERG AND A.-K. TORBERG, *Adaptive quadrature by expansion for layer potential evaluation in two dimensions*, SIAM Journal on Scientific Computing, 40 (2018), pp. A1225–A1249.
- [7] H. ARNOLDUS, *Numerical stabilization of recurrence relations with vanishing solutions*, Computer Physics Communications, 33 (1984), pp. 347–352.
- [8] J. BAGGE, *Accurate quadrature and fast summation in boundary integral methods for Stokes flow*, PhD thesis, KTH Royal Institute of Technology, 2023. ISBN 978-91-8040-608-6.
- [9] J. BAGGE AND A.-K. TORBERG, *Highly accurate special quadrature methods for Stokesian particle suspensions in confined geometries*, International Journal for Numerical Methods in Fluids, 93 (2021), pp. 2175–2224.
- [10] G. BAO, W. HUA, J. LAI, AND J. ZHANG, *Singularity swapping method for nearly singular integrals based on trapezoidal rule*, SIAM Journal on Numerical Analysis, 62 (2024), pp. 974–997.
- [11] A. BARNETT, B. WU, AND S. VEERAPANENI, *Spectrally accurate quadratures for evaluation of layer potentials close to the boundary for the 2D Stokes and Laplace equations*, SIAM Journal on Scientific Computing, 37 (2015), pp. B519–B542.
- [12] A. H. BARNETT, *Evaluation of layer potentials close to the boundary for Laplace and Helmholtz problems on analytic planar domains*, SIAM Journal on Scientific Computing, 36 (2014), pp. A427–A451.
- [13] J. T. BEALE AND S. TLUPOVA, *Extrapolated regularization of nearly singular integrals on surfaces*, Advances in Compu-

- tational Mathematics, 50 (2024), p. 61.
- [14] J.-P. BERRUT AND L. N. TREFETHEN, *Barycentric Lagrange interpolation*, SIAM Review, 46 (2004), pp. 501–517.
  - [15] Å. BJÖRCK AND V. PEREYRA, *Solution of Vandermonde systems of equations*, Mathematics of Computation, 24 (1970), pp. 893–903.
  - [16] V. CALABRESE, A. Q. SHEN, AND S. J. HAWARD, *Naturally derived colloidal rods in microfluidic flows*, Biomicrofluidics, 17 (2023), p. 021301.
  - [17] C. CARVALHO, S. KHATRI, AND A. D. KIM, *Asymptotic approximations for the close evaluation of double-layer potentials*, SIAM Journal on Scientific Computing, 42 (2020), pp. A504–A533.
  - [18] E. CORONA, L. GREENGARD, M. RACHH, AND S. VEERAPANENI, *An integral equation formulation for rigid bodies in Stokes flow in three dimensions*, Journal of Computational Physics, 332 (2017), pp. 504–519.
  - [19] E. CORONA AND S. VEERAPANENI, *Boundary integral equation analysis for suspension of spheres in Stokes flow*, Journal of Computational Physics, 362 (2018), pp. 327–345.
  - [20] M. S. DAVIES WYKES, J. PALACCI, T. ADACHI, L. RISTROPH, X. ZHONG, M. D. WARD, J. ZHANG, AND M. J. SHELLEY, *Dynamic self-assembly of microscale rotors and swimmers*, Soft Matter, 12 (2016), pp. 4584–4589.
  - [21] J. D. DONALDSON AND D. ELLIOTT, *A unified approach to quadrature rules with asymptotic estimates of their remainders*, SIAM Journal on Numerical Analysis, 9 (1972), pp. 573–602.
  - [22] O. DU ROURE, A. LINDNER, E. N. NAZOCKDAST, AND M. J. SHELLEY, *Dynamics of flexible fibers in viscous flows and fluids*, Annual Review of Fluid Mechanics, 51 (2019), pp. 539–572.
  - [23] D. ELLIOTT, B. M. JOHNSTON, AND P. R. JOHNSTON, *Clenshaw–Curtis and Gauss–Legendre Quadrature for Certain Boundary Element Integrals*, SIAM Journal on Scientific Computing, 31 (2008), pp. 510–530.
  - [24] F. FRYKLUND, L. AF KLINTEBERG, AND A.-K. TORNBERG, *An adaptive kernel-split quadrature method for parameter-dependent layer potentials*, Advances in Computational Mathematics, 48 (2022), p. 12.
  - [25] W. GAUTSCHI AND G. INGLESE, *Lower bounds for the condition number of Vandermonde matrices*, Numerische Mathematik, 52 (1987), pp. 241–250.
  - [26] K. M. O. HÅKANSSON, A. B. FALL, F. LUNDELL, S. YU, C. KRYWKA, S. V. ROTH, G. SANTORO, M. KVICK, L. PRAHL WITBERG, L. WÄGBERG, AND L. D. SÖDERBERG, *Hydrodynamic alignment and assembly of nanofibrils resulting in strong cellulose filaments*, Nature Communications, 5 (2014), p. 4018.
  - [27] S. HAO, A. H. BARNETT, P. G. MARTINSSON, AND P. YOUNG, *High-order accurate methods for Nyström discretization of integral equations on smooth curves in the plane*, Advances in Computational Mathematics, 40 (2014), pp. 245–272.
  - [28] J. HELSING AND A. KARLSSON, *An explicit kernel-split panel-based Nyström scheme for integral equations on axially symmetric surfaces*, Journal of Computational Physics, 272 (2014), pp. 686–703.
  - [29] J. HELSING AND R. OJALA, *On the evaluation of layer potentials close to their sources*, Journal of Computational Physics, 227 (2008), pp. 2899–2921.
  - [30] W. R. INC., *Mathematica, Version 13.1*. Champaign, IL, 2022.
  - [31] S. JIANG AND H. ZHU, *Recursive reduction quadrature for the evaluation of laplace layer potentials in three dimensions*, 2024.
  - [32] A. KLÖCKNER, A. BARNETT, L. GREENGARD, AND M. O’NEIL, *Quadrature by expansion: A new method for the evaluation of layer potentials*, Journal of Computational Physics, 252 (2013), pp. 332–349.
  - [33] P. KOLM AND V. ROKHLIN, *Numerical quadratures for singular and hypersingular integrals*, Computers & Mathematics with Applications, 41 (2001), pp. 327–352.
  - [34] P.-S. LAPLACE, *Théorie de Jupiter et de Saturne*, Mémoires de l’Académie royale des sciences de Paris, in Œuvres complètes, tome 11, p. 329, Gauthier-Villars, Paris, 1785.
  - [35] Y. LIU AND A. H. BARNETT, *Efficient numerical solution of acoustic scattering from doubly-periodic arrays of axisymmetric objects*, Journal of Computational Physics, 324 (2016), pp. 226–245.
  - [36] D. MALHOTRA AND A. BARNETT, *Efficient convergent boundary integral methods for slender bodies*, Journal of Computational Physics, 503 (2024), p. 112855.
  - [37] R. OJALA AND A.-K. TORNBERG, *An accurate integral equation method for simulating multi-phase Stokes flow*, Journal of Computational Physics, 298 (2015), pp. 145–160.
  - [38] S. PÅLSSON, M. SIEGEL, AND A.-K. TORNBERG, *Simulation and validation of surfactant-laden drops in two-dimensional Stokes flow*, Journal of Computational Physics, 386 (2019), pp. 218–247.
  - [39] C. POZRIKIDIS, *Boundary integral and singularity methods for linearized viscous flow*, Cambridge University Press, Cambridge, U.K., 1992.
  - [40] S. REDDIG AND H. STARK, *Nonlinear dynamics of spherical particles in Poiseuille flow under creeping-flow condition*, The Journal of Chemical Physics, 138 (2013), p. 234902.
  - [41] M. SIEGEL AND A.-K. TORNBERG, *A local target specific quadrature by expansion method for evaluation of layer potentials in 3D*, Journal of Computational Physics, 364 (2018).
  - [42] C. SORAGENTONE AND A.-K. TORNBERG, *Estimation of quadrature errors for layer potentials evaluated near surfaces with spherical topology*, Advances in Computational Mathematics, 49 (2023), p. 87.
  - [43] S. TLUPOVA AND J. T. BEALE, *Regularized single and double layer integrals in 3D Stokes flow*, Journal of Computational Physics, 386 (2019), pp. 568–584.
  - [44] L. N. TREFETHEN, *Approximation Theory and Approximation Practice, Extended Edition*, Society for Industrial and Applied Mathematics, Philadelphia, PA, 2019.
  - [45] M. WALA AND A. KLÖCKNER, *A fast algorithm for quadrature by expansion in three dimensions*, Journal of Computational Physics, 388 (2019), pp. 655–689.
  - [46] M. WALA AND A. KLÖCKNER, *Optimization of fast algorithms for global Quadrature by Expansion using target-specific expansions*, Journal of Computational Physics, 403 (2020), p. 108976.

- [47] W. YAN, E. CORONA, D. MALHOTRA, S. VEERAPANENI, AND M. SHELLY, *A scalable computational platform for particulate Stokes suspensions*, Journal of Computational Physics, 416 (2020), p. 109524.
- [48] L. YING, G. BIROS, AND D. ZORIN, *A high-order 3D boundary integral equation solver for elliptic PDEs in smooth domains*, Journal of Computational Physics, 219 (2006), pp. 247–275.
- [49] P. YOUNG, S. HAO, AND P. MARTINSSON, *A high-order Nyström discretization scheme for boundary integral equations defined on rotationally symmetric surfaces*, Journal of Computational Physics, 231 (2012), pp. 4142–4159.
- [50] H. ZHU AND S. VEERAPANENI, *High-order close evaluation of Laplace layer potentials: A differential geometric approach*, SIAM Journal on Scientific Computing, 44 (2022), pp. A1381–A1404.

## Appendix A. Proofs.

*Proof of Lemma 2.2.* Let us first focus on the denominator of (2.3). Introduce  $\alpha$  and  $\beta$  such that  $\varphi_0 = \alpha \pm i \ln(\beta)$ , i.e.,

$$(A.1) \quad \alpha = \operatorname{atan2}(y, x), \quad \beta = \frac{\lambda(\theta) + \sqrt{\lambda(\theta)^2 - \rho^2 \sin^2(\theta)}}{\rho \sin(\theta)}.$$

With this notation,  $R^2(\theta, \varphi, \mathbf{x})$  in (1.7) is rewritten as

$$(A.2) \quad \begin{aligned} R^2(\theta, \varphi, \mathbf{x}) &= (a(\theta) \sin(\theta))^2 + \rho^2 + (b(\theta) \cos(\theta) - z)^2 - 2a(\theta) \sin(\theta) (x \cos(\varphi) + y \sin(\varphi)) \\ &= 2a(\theta) (\lambda(\theta) - \rho \sin(\theta) \cos(\varphi - \alpha)), \end{aligned}$$

where  $x = \rho \cos(\alpha)$  and  $y = \rho \sin(\alpha)$ . Next, the numerator of (2.3) is rewritten as

$$(A.3) \quad |e^{i\varphi} - e^{i\varphi_0}|^2 = \left( e^{i\varphi} - \frac{e^{i\alpha}}{\beta} \right) \left( e^{-i\varphi} - \frac{e^{-i\alpha}}{\beta} \right) = 1 + \frac{1}{\beta^2} - \frac{1}{\beta} \cos(\varphi - \alpha).$$

Using that

$$(A.4) \quad \frac{1}{\beta} = \frac{\lambda(\theta) - \sqrt{\lambda(\theta)^2 - \rho^2 \sin^2(\theta)}}{\rho \sin(\theta)}, \quad \frac{1}{\beta^2} = \frac{2\lambda(\theta)}{\rho^2 \sin^2(\theta)} \left( \lambda(\theta) - \sqrt{\lambda(\theta)^2 - \rho^2 \sin^2(\theta)} \right) - 1,$$

Equation (A.3) evaluates to

$$(A.5) \quad |e^{i\varphi} - e^{i\varphi_0}|^2 = \frac{2}{\rho^2 \sin^2(\theta)} \left( \lambda(\theta) - \sqrt{\lambda(\theta)^2 - \rho^2 \sin^2(\theta)} \right) (\lambda(\theta) - \rho \sin(\theta) \cos(\varphi - \alpha)).$$

Finally, combining (A.2) with (A.5) yields

$$(A.6) \quad \begin{aligned} \frac{|e^{i\varphi} - e^{i\varphi_0}|^2}{R^2(\theta, \varphi, \mathbf{x})} &= \frac{1}{a(\theta) \rho^2 \sin^2(\theta)} \left( \lambda(\theta) - \sqrt{\lambda(\theta)^2 - \rho^2 \sin^2(\theta)} \right) \\ &= \frac{1}{a(\theta)} \frac{1}{\lambda(\theta) + \sqrt{\lambda(\theta)^2 - \rho^2 \sin^2(\theta)}}. \end{aligned} \quad \square$$

*Proof of Lemma 2.3.* We rewrite the denominator of the integrand of  $\omega_k^p$  as

$$(A.7) \quad \alpha^2 - 2\alpha \cos(\varphi) + 1 = (1 - \alpha)^2 \left( 1 + \frac{4\alpha}{(1 - \alpha)^2} \sin^2(\varphi/2) \right) = (1 - \alpha)^2 (1 - \ell(\alpha) \sin^2(\varphi/2)),$$

where in the last step  $\ell(\alpha) = -(4\alpha)/(1 - \alpha)^2$  was introduced. By inserting (A.7) into  $\omega_k^p$  and utilizing the periodicity of the integrand, as well as the variable substitution  $t = \varphi/2$  we find

$$(A.8) \quad \omega_k^p(\alpha) = \frac{1}{(1 - \alpha)^{2p}} \underbrace{\int_0^\pi \frac{\cos(2kt)}{(1 - \ell(\alpha) \sin^2(t))^p} dt}_{=: Q_k^p(\alpha)}.$$

The goal is now to derive recurrence formulas for computing the integrals  $Q_k^p$  in (A.8). We will temporarily omit the argument  $\alpha$  of  $\ell$  and  $Q_k^p$ , for ease of notation.

We find,

$$(A.9) \quad Q_k^p = \underbrace{\int_0^\pi \frac{(1 - 2\sin^2(t)) \cos(2(k-1)t)}{(1 - \ell \sin^2(t))^p} dt}_{=: R_k^p} - \underbrace{\int_0^\pi \frac{\sin(2t) \sin(2(k-1)t)}{(1 - \ell \sin^2(t))^p} dt}_{=: S_k^p},$$

where we used the identities  $\cos(2kt) = \cos(2t) \cos(2(k-1)t) - \sin(2t) \sin(2(k-1)t)$ , and  $\cos(2t) = 1 - 2\sin^2(t)$ . We treat the two integrals  $R_k^p$  and  $S_k^p$  separately. Beginning with  $R_k^p$ , adding and subtracting  $(2/\ell)Q_{k-1}^p$  yields

$$(A.10) \quad R_k^p = \frac{2}{\ell} Q_{k-1}^{p-1} + \frac{\ell-2}{\ell} Q_{k-1}^p.$$

Next, using integration by parts,  $S_k^p$  can be expressed as

$$(A.11) \quad S_k^p = -\frac{2(k-1)}{(p-1)\ell} \int_0^\pi \frac{\cos(2(k-1)t)}{(1 - \ell \sin^2(t))^{p-1}} dt = -\frac{2(k-1)}{\ell(p-1)} Q_{k-1}^{p-1},$$

where the boundary term vanished.

Combining (A.10) and (A.11) gives  $Q_k^p$  as

$$(A.12) \quad Q_k^p = \frac{\ell-2}{\ell} Q_{k-1}^p + \frac{4(k-1)}{\ell^2(p-1)} Q_{k-1}^{p-1} = \frac{1+\alpha^2}{2\alpha} Q_{k-1}^p - \frac{(1-\alpha)^2}{2\alpha} \frac{p+k-2}{p-1} Q_{k-1}^{p-1}.$$

In order to compute (A.12), we need the value of  $Q_{k-1}^p$  and  $Q_{k-1}^{p-1}$ . For  $p = 1/2$ , this means that we need  $Q_{k-1}^{-1/2}$ , which we do not have a way of computing. The remedy is to find a relation between  $Q_k^{1/2}$  and  $Q_k^{-1/2}$ .

Consider the special case  $p = 1/2$ . Then, using partial integration and a trigonometric identity, it follows that,

$$(A.13) \quad \begin{aligned} Q_k^{-1/2} &= \frac{\ell}{4k} \int_0^\pi \frac{\sin(2kt) \sin(2t)}{(1 - \ell \sin^2(t))^{1/2}} dt \\ &= \frac{\ell}{8k} \int_0^\pi \frac{\cos(2(k-1)t)}{(1 - \ell \sin^2(t))^{1/2}} dt - \frac{\ell}{8k} \int_0^\pi \frac{\cos(2(k+1)t)}{(1 - \ell \sin^2(t))^{1/2}} dt \\ &= \frac{\ell}{8k} (Q_{k-1}^{1/2} - Q_{k+1}^{1/2}). \end{aligned}$$

Insertion of (A.13) into (A.12) with  $p = 1/2$  gives the recurrence formula

$$(A.14) \quad Q_k^{1/2} = \frac{4(k-1)(\ell-2)}{\ell(2k-1)} Q_{k-1}^{1/2} - \frac{2k-3}{2k-1} Q_{k-2}^{1/2} = \frac{1+\alpha^2}{\alpha} \frac{2(k-1)}{2k-1} Q_{k-1}^{1/2} - \frac{2k-3}{2k-1} Q_{k-2}^{1/2},$$

which, as before, requires  $Q_{k-1}^{1/2}$ , but now also  $Q_{k-2}^{1/2}$ .

Combining (A.12) and (A.14) yields

$$(A.15) \quad Q_k^p(\alpha) = \begin{cases} \frac{1+\alpha^2}{\alpha} \frac{2(k-1)}{2k-1} Q_{k-1}^p - \frac{2k-3}{2k-1} Q_{k-2}^p, & p = 1/2, \\ \frac{1+\alpha^2}{2\alpha} Q_{k-1}^p - \frac{(1-\alpha)^2}{2\alpha} \frac{p+k-2}{p-1} Q_{k-1}^{p-1}, & p > 1/2. \end{cases}$$

The initial values of  $Q_k^p$  for  $p = 1/2, 3/2, 5/2$  are computed using Mathematica [30]. From these initial values a factor  $(1-\alpha)$  appears. Introduce  $\mu_k^p(\alpha) = Q_k^p(\alpha)/(1-\alpha)$ , which inserted into (A.8) gives

$$(A.16) \quad \omega_k^p(\alpha) = \frac{1}{(1-\alpha)^{2p-1}} \mu_k^p(\alpha). \quad \square$$

The recurrence formulas for  $\mu_k^p$  are the same as for  $Q_k^p$  in (A.15). The initial values are scaled by a factor of  $(1-\alpha)$  as compared to the recursion for  $Q_k^p$ .

*Proof of Theorem 2.6.* Inserting (1.7), (2.4), and the result from Lemma 2.2 into (2.19) yields

$$(A.17) \quad u(\mathbf{x}) = \int_0^\pi \frac{1}{a(\theta)^p} \frac{1}{\left(\lambda(\theta) + \sqrt{\lambda(\theta)^2 - \rho^2 \sin^2(\theta)}\right)^p} \left( \int_0^{2\pi} \frac{f(\theta, \varphi)}{|e^{i\varphi} - e^{i\varphi_0}|^{2p}} d\varphi \right) d\theta.$$

Expanding  $f$  in a Fourier series and using (2.8) and Lemma 2.3, the right-most integral in (A.17) can be expressed as

$$(A.18) \quad \int_0^{2\pi} \frac{f(\theta, \varphi)}{|e^{i\varphi} - e^{i\varphi_0}|^{2p}} d\varphi = \frac{\mathcal{F}(\theta)}{(1 - r(\theta))^{2p-1}},$$

where

$$(A.19) \quad \mathcal{F}(\theta) = 2 \sum_{k \in \mathbb{Z}} \hat{f}_k(\theta) e^{ik \operatorname{Re}(\varphi_0)} \mu_k^p(r(\theta)).$$

Out of the complex conjugate pair of roots  $\varphi_0, \bar{\varphi}_0$ , pick the one that has a positive imaginary part. Then, the function  $r$  can be rewritten as

$$(A.20) \quad r(\theta) = \frac{1}{\rho \sin(\theta)} \left( \lambda(\theta) - \sqrt{\lambda(\theta)^2 - \rho^2 \sin^2(\theta)} \right).$$

With this, we find

$$(A.21) \quad \frac{1}{(1 - r(\theta))^{2p-1}} = \left( a(\theta) \frac{\lambda(\theta) + \sqrt{\lambda(\theta)^2 - \rho^2 \sin^2(\theta)}}{R_\lambda^2(\theta, \mathbf{x})} \right)^{p-1/2},$$

where

$$(A.22) \quad R_\lambda^2(\theta, \mathbf{x}) = (a(\theta) \sin(\theta) - \rho)^2 + (b(\theta) \cos(\theta) - z)^2,$$

which upon insertion together with (A.18)-(A.19) into (A.17) gives the desired result.  $\square$

*Proof of Lemma 2.8.* Rewrite the integrals  $\nu_k^p(t_0)$  as

$$(A.23) \quad \nu_k^p(t_0) = \int_{-1}^1 \frac{t^{k-1}}{((t - t_r)^2 + t_i^2)^{p-1/2}} dt.$$

Consider  $p = 3/2$ . Then,

$$(A.24) \quad \begin{aligned} \nu_{k+1}^{3/2}(t_0) &= \int_{-1}^1 \frac{t^{k-2} t^2}{(t - t_r)^2 + t_i^2} dt = \int_{-1}^1 \frac{t^{k-2} ((t - t_r)^2 + t_i^2 + 2t_r t - (t_r^2 + t_i^2))}{(t - t_r)^2 + t_i^2} dt \\ &= \int_{-1}^1 t^{k-2} dt + 2t_r \int_{-1}^1 \frac{t^{k-1}}{(t - t_r)^2 + t_i^2} dt - |t_0|^2 \int_{-1}^1 \frac{t^{k-2}}{(t - t_r)^2 + t_i^2} dt \\ &= \frac{1 - (-1)^{k-1}}{k-1} + 2t_r \nu_k^{3/2}(t_0) - |t_0|^2 \nu_{k-1}^{3/2}(t_0). \end{aligned}$$

By shifting the indices by one, we arrive in the recursion formula in (2.33). The recurrence formula for  $p > 3/2$  is found analogously. Note that if  $t_0 = t_r + it_i$  is purely imaginary, i.e.  $t_r = 0$ , and  $k$  is even, the integrand in (A.23) vanishes due to the odd symmetry of the integrand and the symmetric integration interval.

Lastly, the initial values for  $\nu_k^p(t_0^\lambda)$  in (2.33) for  $p = 3/2, 5/2$ , computed using Mathematica [30], are

$$(A.25) \quad \nu_1^{3/2}(t_0^\lambda) = \begin{cases} \frac{1}{t_i} \left( \tan^{-1} \left( \frac{1 - t_r}{t_i} \right) + \tan^{-1} \left( \frac{1 + t_r}{t_i} \right) \right), & \text{if } t_i \neq 0, \\ \frac{2}{t_r^2 - 1}, & \text{if } t_i = 0, \end{cases}$$

$$(A.26) \quad \nu_2^{3/2}(t_0^\lambda) = \begin{cases} \frac{1}{2} \log \left( 1 - \frac{4t_r}{(1+t_r)^2 + t_i^2} \right) + t_r \nu_0^{3/2}(t_0^\lambda), & \text{if } t_i \neq 0, \\ t_r \nu_1^{3/2}(t_0^\lambda) + \log \left( \frac{t_r - 1}{t_r + 1} \right), & \text{if } t_i = 0, \end{cases}$$

$$(A.27) \quad \nu_1^{5/2}(t_0^\lambda) = \begin{cases} \frac{1}{2t_i^3 ((-1+t_r)^2 + t_i^2) ((1+t_r)^2 + t_i^2)} (2t_i(1-t_r^2 + t_i^2) \\ + (1+t_r^4 + t_i^4) \tan^{-1} \left( \frac{1-t_r}{t_i} \right) - 2(t_i^2 + t_r^2(t_i^2 - 1)) \tan^{-1} \left( \frac{t_r - 1}{t_i} \right)) & \text{if } t_i \neq 0, \\ + ((-1+t_r)^2 + t_i^2) ((1+t_r)^2 + t_i^2) \tan^{-1} \left( \frac{1+t_r}{t_i} \right), \\ \frac{2(1+3t_r^2)}{3(t_r^2 - 1)^3}, & \text{if } t_i = 0, \end{cases}$$

$$(A.28) \quad \nu_2^{5/2}(t_0^\lambda) = \begin{cases} \frac{t_r}{2t_i^3} \left( -\frac{2t_i(-1+|t_0^\lambda|^2)}{t_r^4 + 2t_r^2(-1+t_i^2) + (1+t_i^2)^2} + \tan^{-1} \left( \frac{1-t_r}{t_i} \right) + \tan^{-1} \left( \frac{1+t_r}{t_i} \right) \right), & \text{if } t_i \neq 0, \\ \frac{8t_r}{3(t_r^2 - 1)^3}, & \text{if } t_i = 0. \end{cases} \quad \square$$

**Appendix B. Stabilization of recurrence relations.** As described in Remark 2.5, the recurrence formulas for  $\mu_k^p(\alpha)$  in (2.12) can become numerically unstable due to vanishing solutions being obscured by an exponentially increasing component introduced through round-off errors. In such cases, we employ the numerically stable method proposed in [7], where a three-term recurrence relation is rewritten as a homogeneous tridiagonal matrix equation of size  $k_0 - 1$ . Here,  $k_0$  is chosen such that the solution,  $\mu_k^p(\alpha)$ , is smaller than or equal to the error tolerance  $\epsilon$ . The purpose of this appendix is twofold: to find an error estimate for the forward recurrence error in order to determine if it provides sufficient accuracy, and to determine  $k_0$ .

It turns out that

$$(B.1) \quad \mu_k^p(\alpha) \approx \tilde{\mu}_k^p(\alpha) := C(p) \mu_0^p \alpha^k,$$

where  $C(p)$  is a scaling factor, provides a good estimate of the magnitude of  $\mu_k^p(\alpha)$ . Based on this observation, we construct error estimates for the forward recurrence relations, denoted by  $E_{\text{rec}}^{\text{est}}(\alpha)$ . The expressions for  $\tilde{\mu}_k^p(\alpha)$  and  $E_{\text{rec}}^{\text{est}}(\alpha)$  are presented in Table B.1. In Figure B.1, we compare these estimates with an accurate evaluation of  $\mu_k^p(\alpha)$  for the case  $p = 3/2$ , and note that they are sufficiently accurate. The same conclusion holds for  $p = 1/2$  and  $p = 5/2$ .

Table B.1: Estimates  $\tilde{\mu}_k^p(\alpha)$  of  $\mu_k^p(\alpha)$  and corresponding error estimates of the forwards recurrence formulas in (2.12) for  $p = 1/2, 3/2, 5/2$ .

Layer potential	$p = 1/2$	$p = 3/2$	$p = 5/2$
$\tilde{\mu}_k^p(\alpha)$	$2^{-3} \mu_0^p(\alpha) \alpha^k$	$2^2 \mu_0^p(\alpha) \alpha^k$	$2^4 \mu_0^p(\alpha) \alpha^k$
$E_{\text{rec}}^{\text{est}}(\alpha)$	$\frac{10^{-16}}{2^{-2} \mu_0^p(\alpha) \alpha^k}$	$\frac{10^{-14}}{2^3 \mu_0^p(\alpha) \alpha^k}$	$\frac{10^{-13}}{2^6 \mu_0^p(\alpha) \alpha^k}$

Suppose we want the error in computing  $\mu_k^p(\alpha)$  to be no larger than  $\epsilon$ . Then, if  $E_{\text{rec}}^{\text{est}}(\alpha) \leq \epsilon$ , we compute  $\mu_k^p(\alpha)$  using the corresponding recurrence relation in (2.12). Otherwise, we compute it by solving the tridiagonal matrix system mentioned above. The size of this system is determined by the decay rate of  $\mu_k^p(\alpha)$ . Let  $\bar{k}$  be such that  $\mu_{\bar{k}}^p(\alpha) = \epsilon$ . Then, using (B.1), we estimate

$$(B.2) \quad \bar{k} = \left\lceil \frac{\log \left( \frac{\epsilon}{C(p) \mu_0^p(\alpha)} \right)}{\log(\alpha)} \right\rceil,$$

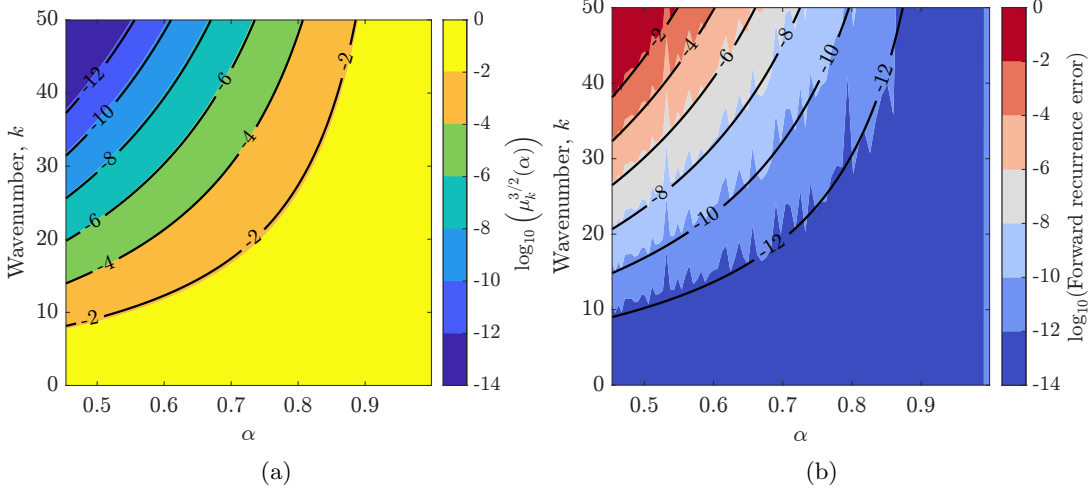


Fig. B.1: Panel (a) shows the value of  $\mu_k^{3/2}(\alpha)$  and panel (b) the associated absolute forward recurrence error. The black lines, illustrating the corresponding estimates in Table B.1 at levels  $10^{-2}$ ,  $10^{-4}$ ,  $10^{-6}$ ,  $10^{-8}$ ,  $10^{-10}$ ,  $10^{-12}$ , agree well with their two counterparts.

where  $\lceil \cdot \rceil$  denotes the ceiling function. In practice, we may require more terms than  $\bar{k}$ . Therefore, we set

$$(B.3) \quad k_0 = \max(\mathcal{S}\bar{k}, k_{\max} + 1, 2),$$

where  $\mathcal{S}$  is a safety factor and  $k_{\max}$  refers to the wavenumber where the Fourier series in (2.5) is truncated. We use  $\mathcal{S} = 1.5$ . By choosing  $k_0$  according to (B.3) the idea is that  $\mu_{k_0}^p(\alpha) \lesssim \epsilon$ .

**Appendix C. Initial guess of centered panel length.** Here we describe how to determine the initial guesses  $\Delta\theta_0$  and  $\Delta\theta_1$  for the secant method used to find the maximum allowed centered panel length  $\Delta\theta_{\max}$  that maintains the error of interest below a specified tolerance  $\epsilon$ . We consider the quadrature and interpolation error estimates in *Error estimate 3.1-3.2* for the function  $\Lambda^{\text{sq}}$  (2.25). Since the procedure is similar for both estimate, we detail only how to set  $\Delta\theta_0$  and  $\Delta\theta_1$  for the interpolation error estimate in *Error estimate (3.2)*.

Let  $\mathbf{x}$  be a target point with root  $\theta_0$  of  $R_\lambda^2(\theta, \mathbf{x})$ . Define  $\theta^* = \text{Re}(\theta_0)$  and let  $\theta_a = \theta^* - \Delta\theta/2$  and  $\theta_b = \theta^* + \Delta\theta/2$  denote the left and right endpoints for a panel centered at  $\theta^*$ , respectively.

If  $\mathbf{x}$  does not fall exactly on the symmetry axis of the geometry, the initial guess  $\Delta\theta_0$  is chosen to be largest possible allowed panel that falls within  $[0, \pi]$ ,

$$(C.1) \quad \Delta\theta_0 = 2 \min(\text{Re}(\theta_0), |\pi - \text{Re}(\theta_0)|),$$

In the case  $\mathbf{x}$  is on the symmetry axis we set  $\Delta\theta_0 = \pi|\text{Im}(\theta_0)|$ , as smaller values of  $\text{Im}(\theta_0)$  generally indicate that  $\mathbf{x}$  is near the surface, resulting in a more pronounced peaked layer potential integrand.

Next, we determine  $\Delta\theta_1$  by simplifying (3.40) to find where it equals  $\epsilon$ . Using  $\beta^I(n, \tau) \approx \Delta\theta|\ell_n(\tau^*)|/2$ , where  $\tau^* = \arg \max_{\tau \in \{-1, 0, 1\}} |\ell_n(\tau)|$ , (3.40) is approximated as

$$(C.2) \quad E_n^I[\Lambda^{\text{sq}}](\Delta\theta) \approx \frac{1}{2\pi} \frac{(L^I - 1)}{|\ell_n(t_0)|} |\ell_n(\tau^*)| \frac{\Delta\theta}{2}.$$

Here,  $t_0 = t(\theta_0, \theta_a, \theta_b)$ , where  $t(\theta, \theta_a, \theta_b)$  is the linear map in (1.6), and  $\ell_n$  is the node polynomial as defined in (3.7). With  $\theta^* = \text{Re}(\theta_0)$ , this mapping transforms  $\theta_0$  into a purely imaginary local root,

$$(C.3) \quad t_0 = is, \quad s = \frac{2|\text{Im}(\theta_0)|}{\Delta\theta}.$$



Assuming  $n$  is even,  $1/\ell_n(is)$  remains real. Using the observation  $\ell_n(z) \approx (z + \sqrt{z^2 - 1})^n / 2^n$  for  $z \in \mathbb{C}$ , (C.2) further reduces to

$$(C.4) \quad \mathbb{E}_n^I[\Lambda^{\text{sq}}](\Delta\theta) \approx \underbrace{\frac{2^{n-1}}{\pi} (L^I - 1) |\ell_n(\tau^*)| |\text{Im}(\theta_0)|}_{=A} s^{-1} \left( s + \sqrt{s^2 + 1} \right)^{-n} \approx A \left( s + \sqrt{s^2 + 1} \right)^{-n} =: F(s)$$

where the last step assumes  $n$  large. We then find  $\Delta\theta_1 = 2|\text{Im}(\theta_0)/s^*|$ , where  $F(s^*) = C$  and  $s^* = (1 - C^{2/n})/(2C^{1/n})$ , with  $C = \epsilon/A$ .

For different values of  $n$  and  $\epsilon$  we find that the secant method usually converges to a strict tolerance within 10 iterations. In the rare cases that it does not converge, Matlab's `fzero` function is used, starting with the initial guess  $\Delta\theta_0$  and, if needed, also with  $\Delta\theta_1$ . If both approaches fail, we set  $\Delta\theta_{\text{max}} = \Delta\theta_0$ .